



Connecting Ly α and Ionizing Photon Escape in the Sunburst Arc

M. Riley Owens¹, Keunho J. Kim^{1,2}, Matthew B. Bayliss¹, T. Emil Rivera-Thorsen³, Keren Sharon⁴, Jane R. Rigby⁵, Alexander Navarre¹, Michael Florian⁶, Michael D. Gladders^{7,8}, Jessica G. Burns¹, Gourav Khullar⁹, John Chisholm¹⁰, Guillaume Mahler^{11,12}, Håkon Dahle¹³, Christopher M. Malhas¹⁰, Brian Welch^{5,14,15}, Taylor A. Hutchison⁵, Raven Gassis¹, Suhyeon Choe³, and Prasanna Adhikari¹

(Sloan Giant Arcs Survey)

¹ Department of Physics, University of Cincinnati, Cincinnati, OH 45221, USA; m.riley.owens@gmail.com

² IPAC, California Institute of Technology, Pasadena, CA 91125, USA

³ The Oskar Klein Centre, Department of Astronomy, Stockholm University, AlbaNova, SE-10691 Stockholm, Sweden

⁴ Department of Astronomy, University of Michigan, 1085 S. University Avenue, Ann Arbor, MI 48109, USA

⁵ Astrophysics Science Division, NASA Goddard Space Flight Center, 8800 Greenbelt Road, Greenbelt, MD 20771, USA

⁶ Steward Observatory, University of Arizona, 933 North Cherry Avenue, Tucson, AZ 85721, USA

⁷ Department of Astronomy & Astrophysics, The University of Chicago, 5640 S. Ellis Avenue, Chicago, IL 60637, USA

⁸ Kavli Institute for Cosmological Physics, University of Chicago, Chicago, IL 60637, USA

⁹ Department of Physics & Astronomy and PITT PACC, University of Pittsburgh, Pittsburgh, PA 15260, USA

¹⁰ Department of Astronomy, The University of Texas at Austin, 2515 Speedway, Stop C1400, Austin, TX 78712, USA

¹¹ Institute for Computational Cosmology, Durham University, South Road, Durham, DH1 3LE, UK

¹² Centre for Extragalactic Astronomy, Durham University, South Road, Durham, DH1 3LE, UK

¹³ Institute of Theoretical Astrophysics, University of Oslo, P.O. Box 1029, Blindern, NO-0315 Oslo, Norway

¹⁴ Department of Astronomy, University of Maryland, College Park, MD 20742, USA

¹⁵ Center for Research and Exploration in Space Science and Technology, NASA Goddard Space Flight Center, 8800 Greenbelt Road, Greenbelt, MD 20771, USA

Received 2024 April 3; revised 2024 October 4; accepted 2024 November 10; published 2024 December 17

Abstract

We investigate the Ly α and Lyman continuum (LyC) properties of the Sunburst Arc, a $z = 2.37$ gravitationally lensed galaxy with a multiply imaged, compact region leaking LyC and a triple-peaked Ly α profile indicating direct Ly α escape. Non-LyC-leaking regions show a redshifted Ly α peak, a redshifted and central Ly α peak, or a triple-peaked Ly α profile. We measure the properties of the Ly α profile from different regions of the galaxy using $R \sim 5000$ Magellan/Magellan Echellette spectra. We compare the Ly α spectral properties to LyC and narrowband Ly α maps from Hubble Space Telescope imaging to explore the subgalactic Ly α –LyC connection. We find strong correlations (Pearson correlation coefficient $r > 0.6$) between the LyC escape fraction ($f_{\text{esc}}^{\text{LyC}}$) and Ly α (1) peak separation v_{sep} , (2) ratio of the minimum flux density between the redshifted and blueshifted Ly α peaks to continuum flux density $f_{\text{min}}/f_{\text{cont}}$, and (3) equivalent width. We favor a complex H I geometry to explain the Ly α profiles from non-LyC-leaking regions and suggest two H I geometries that could diffuse and/or rescatter the central Ly α peak from the LyC-leaking region into our sight line across transverse distances of several hundred parsecs. Our results emphasize the complexity of Ly α radiative transfer and its sensitivity to the anisotropies of H I gas on subgalactic scales. Large differences in the physical scales on which we observe spatially variable direct-escape Ly α , blueshifted Ly α , and escaping LyC photons in the Sunburst Arc underscore the importance of resolving the physical scales that govern Ly α and LyC escape.

Unified Astronomy Thesaurus concepts: Starburst galaxies (1570); Lyman-alpha galaxies (978); Radiative transfer (1335); Strong gravitational lensing (1643)

1. Introduction

Following the formation of the first stars and galaxies, the Universe experienced a phase transition during an era known as the Epoch of Reionization ($z \sim 6$ – 10). Prior to this, protons and electrons sufficiently cooled after the hot Big Bang to recombine ($z \sim 1100$; the Epoch of Recombination) into neutral hydrogen (H I). As the earliest generations of ionizing sources formed, they reionized this neutral gas.

How the Universe reionized remains an outstanding problem of modern astronomy. The two most likely sources of the ionizing radiation (called the Lyman continuum, LyC, with $\lambda < 912 \text{ \AA}$) are star-forming galaxies and active galactic nuclei

(AGN). A drastic reduction in the AGN number density at $z > 6$ (D. Masters et al. 2012; N. Palanque-Delabrouille et al. 2013) might suggest AGN contribute $< 10\%$ (but very likely $< 30\%$) of the reionization “budget” (D. Masters et al. 2012; F. Ricci et al. 2017), but JWST’s discovery of a faint AGN population during and shortly after reionization (D. D. Kocevski et al. 2023; P. Dayal et al. 2024) could challenge this. Other authors have constructed AGN-dominated scenarios consistent with multiple observational constraints (P. Madau & F. Haardt 2015), so the role of AGN in reionization is still controversial.

If star-forming galaxies dominated the reionization of the Universe, LyC photons from ionizing sources in star-forming galaxies must have escaped their host galaxy somehow. However, direct observations of the fraction of LyC which escapes galaxies ($f_{\text{esc}}^{\text{LyC}}$) become increasingly difficult at $z > 2$, and nearly impossible at $z > 4$ (A. K. Inoue et al. 2014). This is because the intergalactic medium (IGM) becomes increasingly

neutral—and therefore increasingly opaque to LyC photons—as we look back beyond $z \sim 2$.

Additionally, various cosmological hydrodynamical simulations disagree on how different sources contributed to reionization and on the dependence of $f_{\text{esc}}^{\text{LyC}}$ on important properties like galaxy mass and redshift (N. Y. Gnedin et al. 2008; X. Ma et al. 2015; M. Sharma et al. 2016; R. Kannan et al. 2022). The dilemma becomes further complicated because the observed timescale of reionization (hundreds of millions of years; e.g., Planck Collaboration et al. 2016) is shorter than expected if the galaxies that caused reionization had similar $f_{\text{esc}}^{\text{LyC}}$ to local galaxies. This discrepancy suggests the LyC production and escape properties measured in local galaxies do not fully describe the processes that drove reionization. If AGN do not dominate reionization, then to satisfy the reionization budget $\gtrsim 10\%$ – 20% of LyC must escape from source galaxies (J. S. Bolton & M. G. Haehnelt 2007; M. Ouchi et al. 2009; M. Kuhlen & C.-A. Faucher-Giguere 2012; B. E. Robertson et al. 2013, 2015; R. J. Bouwens et al. 2015; S. Mitra et al. 2015; V. Khaire et al. 2016; L. C. Price et al. 2016). But LyC surveys consistently find typical escape fractions $\lesssim 10\%$ (E. Vanzella et al. 2010; A. Sandberg et al. 2015; A. Grazian et al. 2016, 2017; L. Guaita et al. 2016; M. J. Rutkowski et al. 2016, 2017; K. Vasei et al. 2016). Although JWST has revealed that some galaxies produce ionizing photons much more efficiently than anticipated (e.g., H. Atek et al. 2024; R. Endsley et al. 2024), which would permit reionization scenarios with lower typical escape fractions, it is unclear if these discrepant galaxies are sufficiently numerous. For a complete review of the current understanding of reionization and JWST’s expected impact, see B. E. Robertson (2022).

One strategy to identify LyC production and escape methods is to observe post-reionization galaxies believed to be good analogs to reionization galaxies (Y. I. Izotov et al. 2011, 2016a, 2017a, 2017b, 2018b, 2019a, 2019b, 2021a; C. C. Steidel et al. 2018; T. J. Fletcher et al. 2019; S. R. Flury et al. 2022a, 2022b; A. J. Pahl et al. 2022; D. Schaerer et al. 2022). Targets at $z \lesssim 4$ avoid the excessive IGM attenuation seen at higher redshift (though it is often still nontrivial), such that rest-LyC radiation is accessible with ultraviolet (UV) or optical filters on ground- and space-based instruments. The primary goal of observing later analogs to reionization galaxies is to link LyC escape to UV diagnostics of a galaxy’s interstellar medium (ISM) and stellar populations, which together strongly regulate the production and escape of LyC photons. Connecting UV diagnostics and LyC is vital because the nonionizing UV to rest-optical is the wavelength band JWST (and soon the generation of extremely large telescopes, ELTs) directly accesses from reionization galaxies (A. J. Bunker et al. 2023; S. Mascia 2023; H. Williams et al. 2023; Y.-H. Lin et al. 2024). The relations between UV diagnostics and $f_{\text{esc}}^{\text{LyC}}$ established in lower-redshift analogs can then constrain $f_{\text{esc}}^{\text{LyC}}$ for reionization galaxies and the primary escape methods of LyC photons.

The overarching strategy to find analogs to reionization galaxies is to preselect LyC-leaking candidates based on indirect tracers of LyC escape (e.g., the [O III] 4959, 5007 Å/[O II] 3727, 3729 Å ratio O32 or Ly α peak separation v_{sep}). In this fashion, many post-reionization LyC leakers have been identified (N. Bergvall et al. 2006; E. Leitert et al. 2011, 2013; S. Borthakur et al. 2014; R. E. Mostardi et al. 2015; S. de Barros et al. 2016; Y. I. Izotov et al.

2016b, 2016c, 2018a, 2018c, 2020, 2021b, 2022; C. Leitherer et al. 2016; A. E. Shapley et al. 2016; F. Bian et al. 2017; J. Puschignig et al. 2017; C. C. Steidel et al. 2018; E. Vanzella et al. 2018; T. J. Fletcher et al. 2019; Z. Ji et al. 2020; K. Saha et al. 2020; L. H. Jones et al. 2021; M. A. Malkan & B. K. Malkan 2021; R. Marques-Chaves et al. 2021, 2022; A. Saxena et al. 2022; S. R. Flury et al. 2022a, 2022b), though generally with insufficient spatial resolution to resolve the small scales (down to tens of parsecs and less) expected to dictate LyC escape. Notably, T. E. Rivera-Thorsen et al. (2022) conducted a bottom-up search for LyC sources selected solely by their LyC emission in archival Hubble Space Telescope (HST) imaging that suggested the preselection criteria normally imposed in LyC emitter searches may miss nontrivial contributors to the ionizing background.

This search for tracers of LyC escape, spurred by the simultaneous necessity to understand the process of reionization and inability to directly observe LyC from reionization, makes the galaxy PSZ1-ARC G311.6602-18.4624—nicknamed the Sunburst Arc by T. E. Rivera-Thorsen et al. (2017)—a compelling target to study LyC escape. The Sunburst Arc is a strongly lensed (magnifications between $\sim 10\times$ and $100\times$; T. E. Rivera-Thorsen et al. 2019; G. V. Pignataro et al. 2021; K. Sharon et al. 2022) galaxy arc at redshift $z \approx 2.37$. Discovered by H. Dahle et al. (2016), the Sunburst Arc has garnered great interest because of (1) its high LyC escape fraction (T. E. Rivera-Thorsen et al. 2017, 2019; E. Vanzella et al. 2022), (2) the unique mode of LyC escape implied by its Ly α emission, and (3) the advantages offered by the strong lensing in studying LyC escape. The foreground galaxy cluster PSZ1 G311.65-18.48 at $z \approx 0.44$ lenses the Sunburst Arc into 12 full or partial images of the galaxy that show at least 54 individual features in total (G. V. Pignataro et al. 2021; K. Sharon et al. 2022). Some of these images could represent individual star clusters with radii as small as $\lesssim 20$ pc (E. Vanzella et al. 2022). A compact LyC-emitting region appears at least 12 times (T. E. Rivera-Thorsen et al. 2019), and may be less than 10 pc across (U. Mestric et al. 2023).

Previous studies strongly disfavor the presence of an AGN in the Sunburst Arc (T. E. Rivera-Thorsen et al. 2019; R. Mainali et al. 2022). Instead, past work favors young, massive stars produced in a recent burst of star formation as being responsible for the observed LyC photons, mainly evidenced by the P-Cygni wind profiles, high-velocity and highly ionized galactic outflows, and compact regions with extremely blue UV slopes characteristic of hot, young stellar populations (T. E. Rivera-Thorsen et al. 2017, 2019; J. Chisholm et al. 2019; R. Mainali et al. 2022; K. J. Kim et al. 2023; U. Mestric et al. 2023; M. Pascale et al. 2023). Together, the excellent spatial resolution in the source plane, multiple lines of sight into the galaxy, high signal-to-noise ratio (SNR), and young stellar populations make the Sunburst Arc an ideal target to understand how LyC photons may have escaped from earlier star-forming galaxies during reionization.

A promising tool to investigate LyC escape is a source’s Ly α emission (see, e.g., A. Verhamme et al. 2015). Ly α photons primarily originate from recombining H II ions and free electrons in H II regions around massive OB stars producing copious LyC photons, implying that Ly α and LyC photons begin their journeys not far from each other. As a resonant emission line of H I, Ly α photons interact strongly with the same gas that attenuates LyC from sources within a galaxy (stronger, in fact, than LyC; B. T. Draine 2011). So, the intricate radiative transfer of Ly α (for a review, see, e.g.,

M. Dijkstra 2017) encodes complex information about the H I that LyC photons must navigate to escape the galaxy. Though H I governs the paths of Ly α and LyC photons, both are sensitive to significantly different column densities (e.g., for $\tau = 1$, $\log_{10}(N_{\text{HI}} [\text{cm}^{-2}]) \sim 13.8$ and $\log_{10}(N_{\text{HI}} [\text{cm}^{-2}]) \sim 17$ for Ly α and LyC photons, respectively). The different column density sensitivities, coupled with the resonant nature of Ly α , necessitates different interpretation approaches for Ly α and LyC signatures. LyC photons travel along a sight line until being destroyed by intervening material (H I or dust), but H I can rescatter Ly α photons many times (provided dust does not destroy those Ly α photons). And crucially, unlike Ly α photons, LyC photons are not strongly sensitive to the kinematics of H I. This means Ly α photons may not actually follow the observed sight lines, and could have originated from a different physical region than observed. So, Ly α properties do not necessarily correspond with the areas that they appear to come from, and may appear diffused to a much larger area than the progenitor H II regions (e.g., M. Hayes et al. 2014; G. Östlin et al. 2014; T. E. Rivera-Thorsen et al. 2015; E. C. Herenz et al. 2016; J. S. Bridge et al. 2018; A. Rasekh et al. 2022; J. Melinder et al. 2023).

Because of the complex connection between the regulation of Ly α and LyC photon escape, one of the Sunburst Arc’s most remarkable features is its triple-peaked Ly α profile, which we investigate in this work. T. E. Rivera-Thorsen et al. (2017) first reported this feature, originally predicted by C. Behrens et al. (2014), and seldom observed in other galaxies (Y. I. Izotov et al. 2018c; E. Vanzella et al. 2018, 2020a). As we present, with one exception, all observations of triple-peaked Ly α profiles in the Sunburst Arc seem associated with the LyC-leaking region. So, this unique Ly α profile may be connected to LyC escape. Observations and radiative transfer models of Ly α often explain this unique profile with a perforated covering shell of H I that permits direct escape of Ly α and LyC photons through one or several holes, but otherwise scatters (attenuates) Ly α (LyC) photons (C. Behrens et al. 2014; A. Verhamme et al. 2015; T. E. Rivera-Thorsen et al. 2015, 2017).

In this work, we analyze rest-UV and rest-optical observations of the Sunburst Arc from slit spectroscopy with Magellan/Magellan Echellette (MagE; Section 2.1) and archival multifilter imaging with HST (Section 2.2). We specifically study the Ly α properties of regions of the galaxy and their $f_{\text{esc}}^{\text{LyC}}$ to build a physical picture of how Ly α and LyC photons escape the galaxy. To accomplish this, we fitted the Ly α spectra (Section 3.5) and calculated estimates of $f_{\text{esc}}^{\text{LyC}}$ in the spectroscopic apertures from the HST imaging (Section 3.4). We compare common Ly α parameters to determine their mutual dependence and relation to LyC escape (Section 4). In Section 5, we present several hypotheses to explain the spatial variation of the Ly α velocity profiles and their connection to LyC escape, ultimately favoring unique source-plane H I morphologies as causative mechanisms for the observed Ly α and LyC signatures. We conclude in Section 6 with implications for future Ly α and LyC observations in lensed galaxies.

Throughout this work, we assume a flat Lambda cold dark matter (Λ CDM) cosmology with $H_0 = 70 \text{ km s}^{-1} \text{ Mpc}^{-1}$, $\Omega_m = 0.3$, and $\Omega_\Lambda = 0.7$.

2. Observations

This work used rest-frame Ly α spectra from Magellan/MagE (Section 2.1) as well as HST imaging (Section 2.2) of the rest-frame Ly α (HST/WFC3 F410M), LyC (HST/WFC3 F275W), near-UV continuum (HST/ACS F814W; WFC3 F390W, F555W, F606W) and rest-frame optical narrowband (HST/WFC3 F128N, F153M). See Tables 1 and 2 for descriptions of the respective Magellan and HST observations.

2.1. Magellan Spectroscopy

We observed nine locations on the two largest arcs of the Sunburst Arc (Figure 1) in the observed-frame optical ($\sim 3200 - 8500 \text{ \AA}$) wavelengths with the MagE spectrograph (J. L. Marshall et al. 2008) mounted on the Magellan I Baade Telescope (6.5 m) at the Las Campanas Observatory in Chile. These spectra cover the rest-UV ($\sim 950 - 2500 \text{ \AA}$, including Ly α) at the redshift of the Sunburst Arc. Apart from slit M0, which predated the acquisition of HST imaging, we compared the MagE slit viewing camera to HST images to precisely position the slits along the arc. M0 simply targeted the brightest part of the arc as measured in discovery imaging from the European Southern Observatory’s New Technology Telescope (H. Dahle et al. 2016). Of the nine apertures, the HST imaging reveals that five apertures target images of the LyC-leaking region and four do not. One slit (M3) covers an unusual, highly magnified object (image 4.8 in Figures 1 and 4) previously discussed by E. Vanzella et al. (2020b), J. M. Diego et al. (2022), K. Sharon et al. (2022), M. Pascale & L. Dai (2024), and S. Choe et al. (2024), favored to be a supernova by E. Vanzella et al. (2020b) and later a luminous blue variable (LBV) star in outburst by J. M. Diego et al. (2022). K. Sharon et al. (2022) presented evidence the unusual source is not a transient event, and is likely due to an unusual lensing configuration, as suggested by J. M. Diego et al. (2022). Table 1 summarizes the MagE pointings. J. R. Rigby et al. (in preparation) will present the full observation log for each pointing. The MagE data were reduced following the same methods as described in J. R. Rigby et al. (2018). Slits M0 and M3 and two conglomerate stacked spectra are the only previously published portions of these MagE observations (first published in T. E. Rivera-Thorsen et al. 2017, S. Choe et al. 2024, and R. Mainali et al. 2022, respectively). The reduction procedure of the new data presented here is identical to the reduction for slit M0 published in T. E. Rivera-Thorsen et al. (2017). The MagE observations of Ly α appear in Figure 2.

2.2. Hubble Space Telescope Imaging

We adopted some HST data used in this work as reduced and presented in other works: the ACS F814W and WFC3 F390W, F410M, F555W, and F606W observations in K. Sharon et al. (2022), and the WFC3 F128N and F153M observations in K. J. Kim et al. (2023).

We analyzed new, ultra-deep rest-LyC images, adding 26 additional orbits of F275W (GO-15949, PI: M. Gladders) to the three orbits of F275W (GO-15418, PI: H. Dahle) previously presented in T. E. Rivera-Thorsen et al. (2019), resulting in a total of 29 orbits (86.9 ks) of integration time. The new F275W observations were structured in visits of typically three orbits, with two full-orbit integrations to minimize effects of charge transfer inefficiency, and two half-orbit integrations, providing a total of four frames to ensure good cosmic-ray rejection and point-spread function (PSF) reconstruction in each visit.

Table 1
MagE Observation Log and Magnifications

Slit	Position (hh:mm:ss, dd:mm:ss)	Width (arcsec)	Date (UT)	Exp. Time (ks)	FWHM (arcsec)	R	μ
M5	(15:50:01.1649, -78:11:07.822)	0.85	2018 Apr 22	13.5	0.97	5500 ± 400	51_{-10}^{+5}
M4	(15:50:04.9279, -78:10:59.032)	0.85	2018 Apr 21	7.2	0.71	5400 ± 300	$14.6_{-3}^{+0.8}$
M6	(15:50:06.6389, -78:10:57.412)	0.85	2018 Apr 22, 23	12.9	0.76	5300 ± 300	147_{-20}^{+5}
M3	(15:50:00.6009, -78:11:09.912)	0.85	2018 Apr 21	12	0.70	5500 ± 400	36_{-5}^{+4a}
M0	(15:50:04.4759, -78:10:59.652)	1	2017 May 24	13.5	1.34	4700 ± 200	10_{-7}^{+10}
M2	(15:49:59.7480, -78:11:13.482)	0.85	2018 Apr 21, 23	8.1	0.77	5300 ± 300	32_{-3}^{+6}
M7	(15:50:07.3959, -78:10:56.962)	0.85	2018 Aug 11, 12	14.4	0.73	5200 ± 200	35_{-6}^{+3}
M8	(15:49:59.9499, -78:11:12.242)	0.85	2018 Aug 10, 11, 12	14.4	0.70	5200 ± 300	29_{-3}^{+6}
M9	(15:50:00.3719, -78:11:10.512)	0.85	2018 Apr 23	13.5	0.68	5500 ± 400	31_{-3}^{+4}

Notes. From left to right: slit label; position in R.A. (hh:mm:ss), decl. (dd:mm:ss) (J2000); slit width in arcseconds; observation date (UT); total exposure time (in kiloseconds); individual exposure-time-weighted average of the seeing conditions (in arcseconds); median spectral resolution (R) as determined by the widths of night sky lines; and average magnification (μ) as calculated using the lens model of K. Sharon et al. (2022).

^a Although slit M3 captures an extremely magnified region of the galaxy, the quoted magnification is puzzlingly nonextreme because the extreme magnification relies upon a postulated, unseen perturbing mass (likely detected in JWST/NIRCam imaging by S. Choe et al. 2024), the effect of which is not included in the model used to calculate the magnifications listed here.

Table 2
HST Observations

Camera	Filter	λ_{pivot} (Å)	Width (Å)	t_{exp} (s)	Purpose	Program
ACS	WFC/F814W	8333	2511	5280	$f_{\text{esc}}^{\text{LyC}}$, SED fit	GO-15101
WFC3	IR/F128N	12832	159	16818	SED fit	GO-15949
	IR/F153M	15322	685	5612	SED fit	GO-15949
	UVIS/F275W	2710	405	5413	$f_{\text{esc}}^{\text{LyC}}$	GO-15418
	UVIS/F275W	81489	$f_{\text{esc}}^{\text{LyC}}$	GO-15949
	UVIS/F390W	3924	894	3922	Ly α off-band	GO-15949
	UVIS/F410M	4109	172	13285	Ly α on-band	GO-15101
	UVIS/F555W	5308	1565	5616	Ly α off-band, SED fit	GO-15101
	UVIS/F606W	5889	2189	5830	SED fit	GO-15377

Note. HST observations used in this work. From left to right: HST instrument; filter; pivot wavelength of filter (in angstroms); filter width (in angstroms); exposure time (in seconds); purpose for this work; and program ID.

Individual processed frames were taken from the Mikulski Archive for Space Telescopes (MAST) and stacked using the tools in the `DrizzlePac` package. The final stacked image was astrometrically referenced to the F606W imaging, with a pixel scale of $0''.03 \text{ pixel}^{-1}$ and a 0.6 pixel Gaussian drizzle drop size. The deeper exposures achieve a 5σ depth of $m_{\text{AB}} \approx 29.9$ (compared to the corresponding 5σ depth of $m_{\text{AB}} \approx 28$ from the shallower exposures in T. E. Rivera-Thorsen et al. 2019) but do not reveal any new LyC-leaking images or LyC morphology than presented in T. E. Rivera-Thorsen et al. (2019). Figure 4 shows the new LyC maps of the two main segments of the Sunburst Arc targeted by this work’s MagE slit apertures. Table 2 summarizes the HST observations used in this work.

All the HST data used in this paper can be found in MAST doi:10.17909/t87g-a816.

3. Data Analysis

3.1. Redshifts

We adopted the spectroscopic redshifts presented by R. Mainali et al. (2022, Table 1 therein), measured from the

narrow component of the strong rest-optical nebular emission line [O III] 5007 Å of the MagE targets, captured with the Folded-port InfraRed Echellette (FIRE; R. A. Simcoe et al. 2013) mounted on the Magellan I Baade Telescope. See Figure 1 in R. Mainali et al. (2022) for a comparison between the FIRE and MagE pointings (all the MagE pointings discussed in this paper have overlapping FIRE pointings) and their Section 3.3 for a description of how they computed the redshifts of the targeted regions of the galaxy. We did not adopt a single redshift for the galaxy because it is critical to accurately place each MagE spectrum into the rest frame while stacking the spectra, for example, or accurately determining peculiar velocities.

3.2. Stacking Spectra

T. E. Rivera-Thorsen et al. (2019) identified the LyC-leaking images in the Sunburst Arc as a compact, star-forming region, which R. Mainali et al. (2022) used to justify stacking the MagE spectra of the LyC-leaking and non-LyC-leaking images to compare the two sets of regions. We repeated this stacking (labeling the stacked LyC-leaking and non-LyC-leaking spectra as “L” and “NL,” respectively), but excluded slit M0 from the

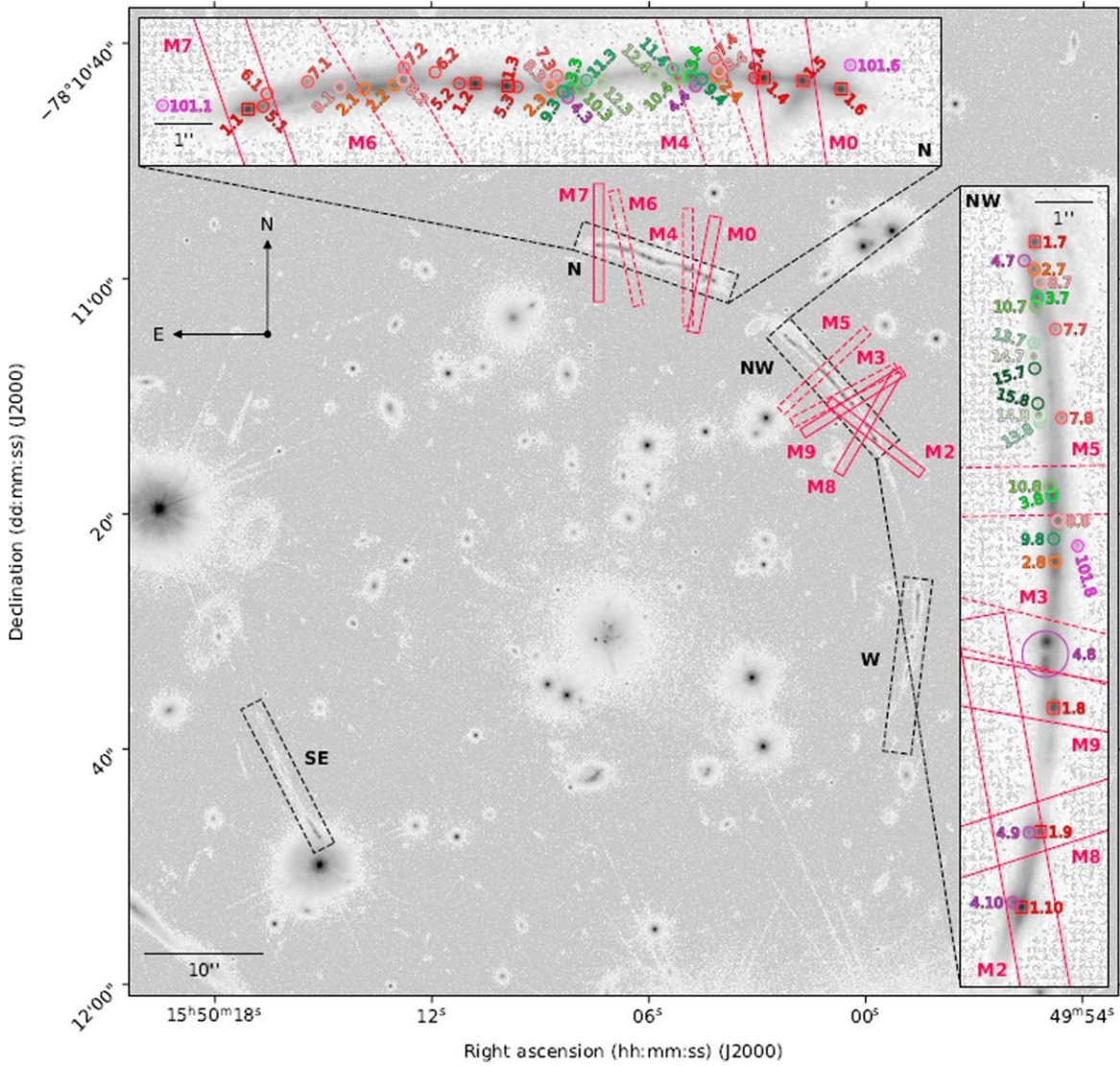


Figure 1. HST/WFC3 F606W imaging of the Sunburst Arc from GO-15377 (PI: M. Bayliss). Black dashed rectangles on the main image mark the main arc segments, labeled as in K. Sharon et al. (2022). The inset panels enlarge the two largest arcs, which are the focus of spectroscopic MagE data presented in this work (Table 1). The MagE apertures appear as magenta rectangles, where solid apertures cover images of the LyC-leaking region, and dashed apertures do not. In the inset panels, circles (except for squares for the LyC-leaking region) mark images of different source-plane regions of the Sunburst Arc, as labeled and colored in the lens model of K. Sharon et al. (2022).

LyC-leaking stack due to the poor observing conditions (see Table 1) that prevented an accurate fluxing, and the presence of a foreground galaxy in the aperture (see the diffuse emission southeast of image 1.5 in Figure 1), and also excluded slit M3 from either stack, as it includes a bright image of an extremely magnified area of the galaxy (J. M. Diego et al. 2022; K. Sharon et al. 2022) that may not be representative of the broader region it is embedded in (see Section 5.1 for more details). To create the stacks, we normalized the individual spectra used to create a stack by their median flux density between 1267 and 1276 Å in the rest frame, interpolated them to a common set of identically sized wavelength bins, and then averaged their flux densities at each bin. Figure 3 shows the stacked Ly α spectra.

3.3. Creating Narrowband Ly α Maps

To supplement the spectroscopic Ly α data with spatial Ly α information, we created Ly α images by estimating the

contribution of Ly α to the emission observed in the F410M filter using an approach similar to that described in Section 2.5 of K. J. Kim et al. (2023). We fit spectral energy distribution (SED) models to the integrated F153M, F128N, F814W, F606W, and F555W photometry of four images of the multiply imaged source galaxy, which include flux from image families 3, 4, 8, 9, and 10 (using the nomenclature of K. Sharon et al. 2022). These four fits should produce nearly identical SEDs because they are fit to different lensed images of the same source. Fitting four different SEDs provides a direct estimate of any systematic variations caused by differential magnification between the different emission clumps in the lensed galaxy.

We used PROSPECTOR, a Markov Chain Monte Carlo–based stellar population synthesis and parameter inference framework (C. Conroy & J. E. Gunn 2010; D. Foreman-Mackey et al. 2013; B. D. Johnson et al. 2021) to fit SED models with a delayed- τ (with age and the e -folding time of the star formation rate as free parameters) + constant star formation model, and also fitted for stellar mass, dust attenuation (using the Calzetti

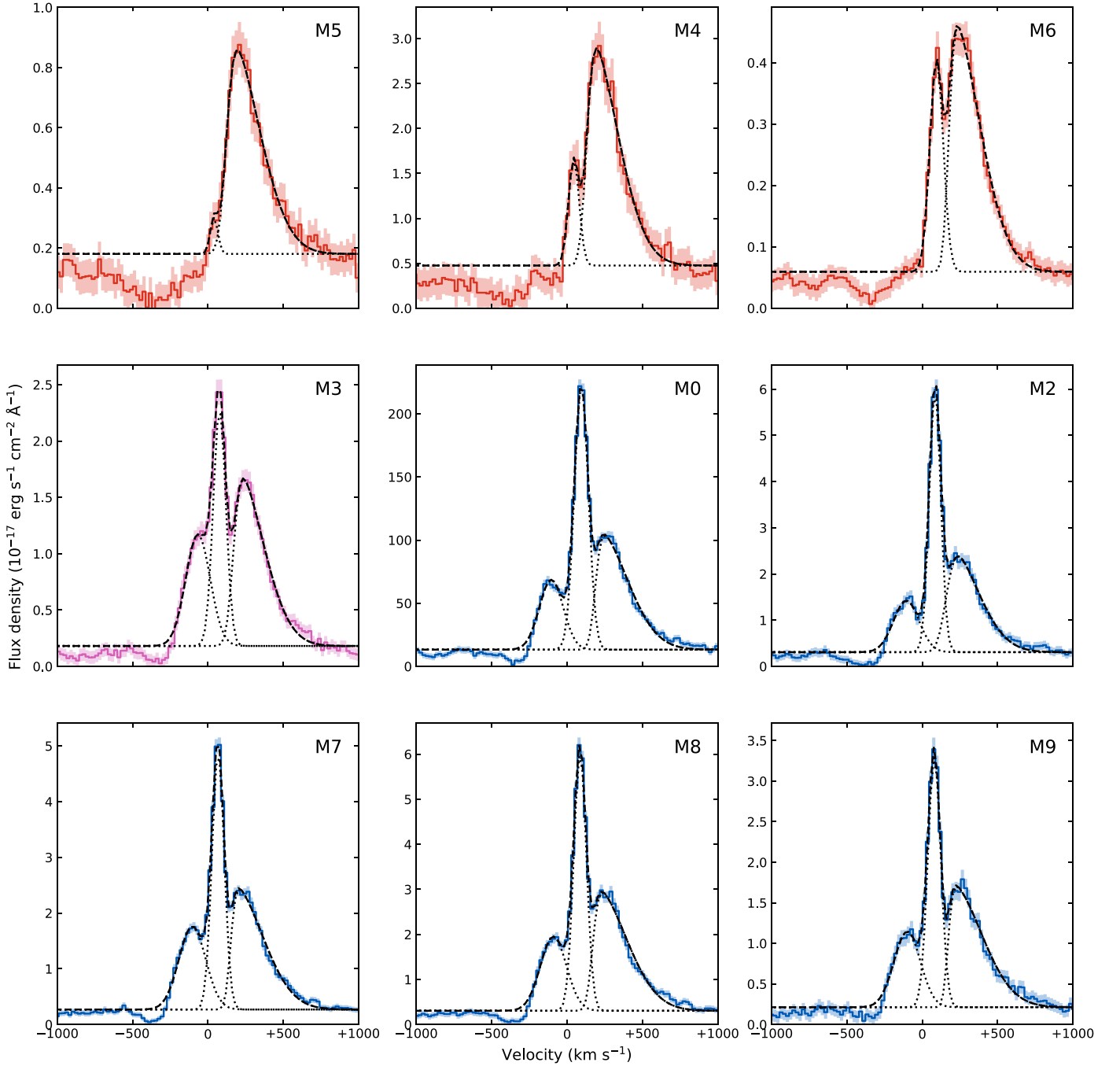


Figure 2. The magnification-corrected, rest-frame Ly α profiles, ordered from left to right, then top to bottom, first by increasing central Ly α peak strength relative to the redshifted Ly α peak in the non-LyC-leaking apertures, then the LyC-leaking apertures by the numeric order of their slit identifier. Those in red (top row) are non-LyC-leaking apertures (slits M5, M4, and M6), in pink (slit M3) is a non-LyC-leaking aperture targeting a highly magnified, exotic object (see Section 5.1 for more details), and in blue are the LyC-leaking apertures (slits M0, M2, M7, M8, and M9). The dashed black lines represent the overall fits, and dotted black lines represent the individual Ly α peak fits, based on the median best-fit parameters from the fitting described in Section 3.5.4. The shaded region represents the 2σ uncertainties of the flux densities. The observations clearly show a significant variety of Ly α profiles in the Sunburst Arc. Slit M0 has a much larger flux density scale due to poor observing conditions that prevented an accurate fluxing (see Table 1 for more details about the observation).

attenuation model), and the gas ionization parameter $\log U$. We used a fixed value for stellar metallicity ($\log(Z/Z_{\odot}) = -0.33$, informed by spectroscopy), and a Kroupa initial mass function (P. Kroupa 2001), and evaluated nebular continuum and line emission via the CLOUDY component of the embedded Flexible Stellar Population Synthesis (B. Johnson et al. 2022) framework (see N. Byler et al. 2017 for details). We took the stellar and nebular continuum from the highest-posterior-probability SED model as a proxy for the true continuum. The SEDs and

filter transmission curves (except F606W and F814W) appear in Figure 7 of K. J. Kim et al. (2023). We corrected the SEDs for Milky Way dust extinction according to the three-dimensional interstellar dust extinction map of G. M. Green et al. (2015).

These SEDs did not model attenuation from the Ly α forest, which may cause an oversubtraction of the continuum. To test if this was an issue, we normalized each SED at an observed wavelength of 1 μm and compared the SED count rates in the

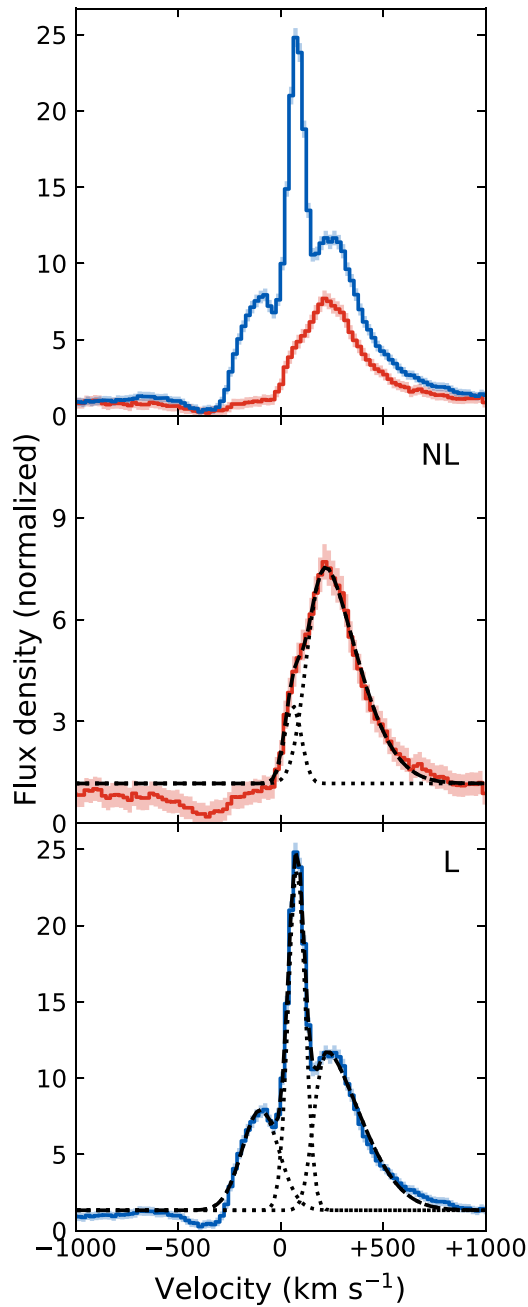


Figure 3. $\text{Ly}\alpha$ profiles of the stacked LyC-leaking and non-LyC-leaking MagE slit apertures with fits. Top: $\text{Ly}\alpha$ profiles of the stacked LyC leaker (above in blue) and non-LyC-leaking regions (below in red). The shaded regions indicate the 3σ uncertainty of the flux density. Center: stacked $\text{Ly}\alpha$ profile of the non-LyC-leaking apertures with the total fit in dashed black and individual peak fits in dotted black. Bottom: stacked LyC leaker $\text{Ly}\alpha$ profile with the total fit in dashed black and individual peak fits in dotted black.

on-band (on- $\text{Ly}\alpha$) F410M filter with the count rates predicted for F410M from the stacked MagE LyC-leaking and non-LyC-leaking spectra after masking out $\text{Ly}\alpha$ and other emission lines, and convolving the data with a boxcar kernel. We found no significant difference between the predicted F410M continuum count rates from the SED fitting and the $\text{Ly}\alpha$ -removed, scaled MagE spectra.

We calculated the $\text{Ly}\alpha$ emission as the $\text{Ly}\alpha$ flux equal to on-band flux minus off-band flux \times a scaling factor. We estimated the scaling factor as the mean of the individual scaling factors of the different continuum models described above. We used

the standard deviation of the individual scaling factors of the models as an estimate of the systematic uncertainty in the scaling factor. We estimated the statistical uncertainty in the continuum subtraction from regions of empty sky in the data. We made two maps: one with F390W as the off-band filter, which samples continuum closer to $\text{Ly}\alpha$ but includes $\text{Ly}\alpha$ and $\text{Ly}\alpha$ -forest-attenuated continuum, and one with F555W as the off-band filter, which samples continuum farther from $\text{Ly}\alpha$. Figure 4 shows the $\text{Ly}\alpha$ maps of the two segments of the Sunburst Arc for both off-band filter choices. We report uncertainties of measurements made from the $\text{Ly}\alpha$ maps with the combined systematic and statistical uncertainties.

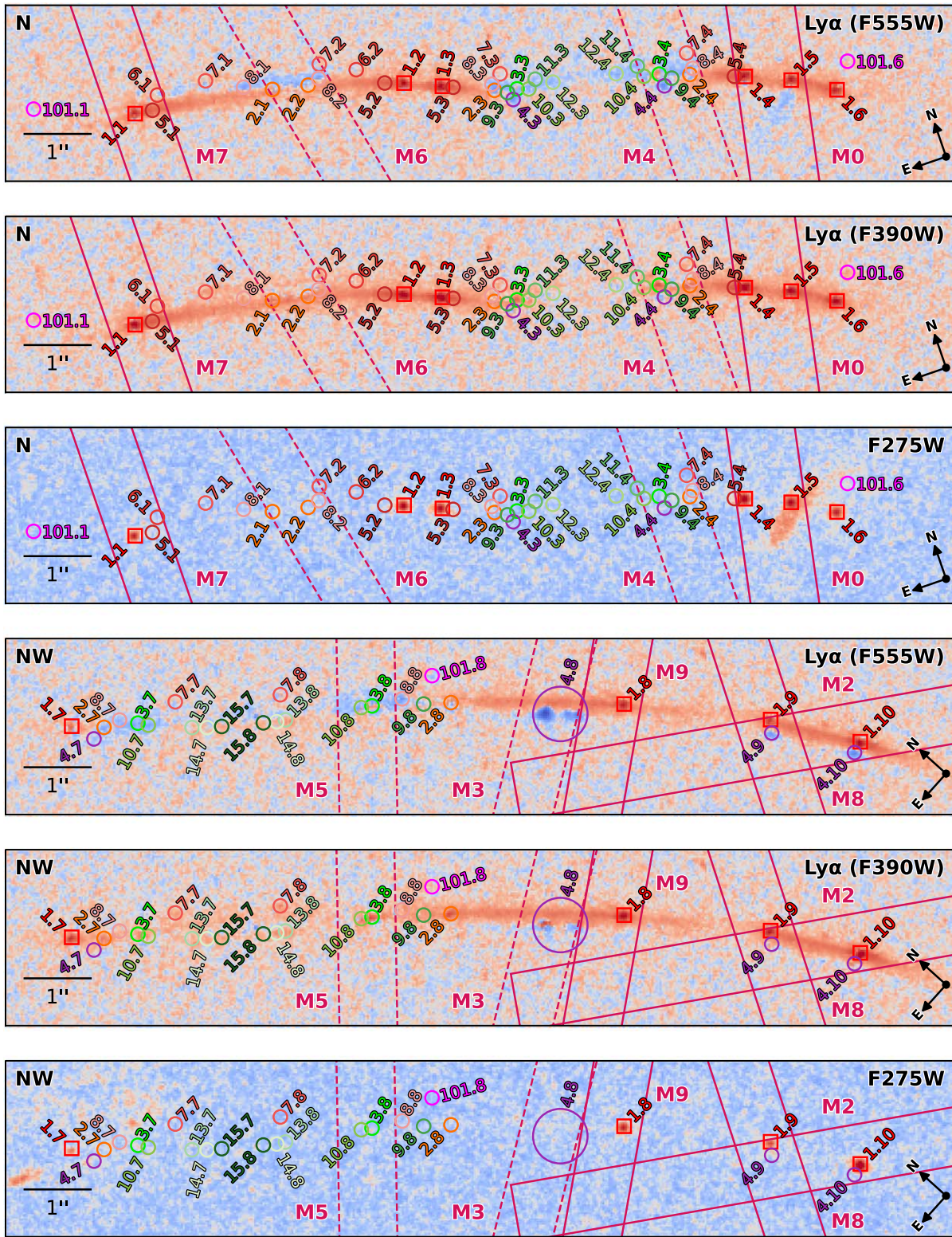
3.4. Measuring $f_{\text{esc}}^{\text{LyC}}$

T. E. Rivera-Thorsen et al. (2019) previously computed $f_{\text{esc}}^{\text{LyC}}$ for the images of the LyC-leaking region, and more recently M. Pascale et al. (2023) indirectly estimated the LyC-leaking region's $f_{\text{esc}}^{\text{LyC}}$ from the observed nebular continuum and nebular line strengths. The MagE apertures include five slits that cover six of the LyC-leaking images investigated in T. E. Rivera-Thorsen et al. (2019), but also four slits that only cover images of the galaxy that do not leak LyC (Figure 1). We computed the IGM-unattenuated, absolute LyC escape fraction $f_{\text{esc}}^{\text{LyC}}$ within each MagE aperture. We adapted the method that T. E. Rivera-Thorsen et al. (2019) used to calculate the apparent, relative LyC escape fraction, summarized in their Equation S3. Briefly, they used the nonionizing rest-UV continuum F814W observations (unaffected by H I absorption) in tandem with theoretical, intrinsic Starburst99 (C. Leitherer et al. 1999) spectra to compute the expected flux in F275W if the sight line was completely transparent to LyC. To instead compute the IGM-unattenuated, absolute LyC escape fractions, we shifted the IGM transmission factor in their Equation S3 to the opposite side of the equation and used dust-extinguished Starburst99 spectra instead of the intrinsic Starburst99 spectra.

To prepare the F275W and F814W images to measure the necessary photometry, we (1) removed a foreground interloping galaxy, and (2) subtracted the background level from the images. The foreground galaxy is bright in F275W, contaminating slit M0 (see the diffuse emission southeast of image 1.5 in Figure 1). We subtracted the galaxy from the F275W and F814W imaging with the galaxy surface brightness profile modeling software GALFIT (C. Y. Peng et al. 2010). We fitted the galaxy with a single Sérsic profile in both F275W and F814W. We computed PSF models for both bands using in-field stars. The GALFIT results appear in Figure 5.

The summed F275W flux in a MagE aperture is sensitive to the background level of the drizzled image (and thus so is $f_{\text{esc}}^{\text{LyC}}$). Background level overestimates will underpredict $f_{\text{esc}}^{\text{LyC}}$, while underestimates will overpredict $f_{\text{esc}}^{\text{LyC}}$. To accurately model the complex background level, we used the Python Photutils package (L. Bradley et al. 2022). We iterated the background modeling parameters until the F275W flux in the non-LyC-leaking apertures was consistent with minimal flux.

Although these steps make the images ready for photometry measurements, unlike T. E. Rivera-Thorsen et al. (2019), this work aims to closely compare LyC escape fractions to spectroscopic properties. The LyC escape fractions are measurable on a much smaller scale than the spectroscopic properties, since the latter are associated with a slit aperture (to compare, T. E. Rivera-Thorsen et al. 2019 used square apertures ~ 0.1 arcsec across to measure photometries of images, as



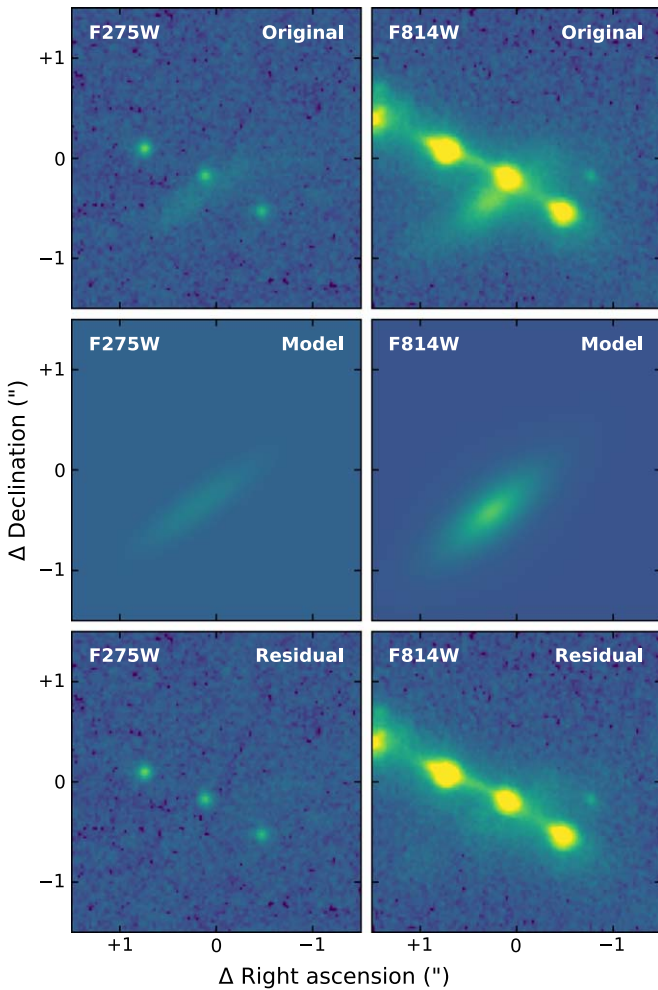


Figure 5. Results of using GALFIT to remove a foreground galaxy over an image of the LyC leaker (image 1.5 in Figure 1) from the F275W and F814W images. Each column uses the same color map with a cube root scale, with minima (maxima) of the masked median of the cutout minus $2\times$ (plus $100\times$) the standard deviation of the source-masked cutout. The GALFIT models have a flat background of zero.

accounting for the air mass of each exposure of each slit aperture (J. R. Rigby et al. in preparation). We then measured the F275W and F814W fluxes associated with the LyC escape fraction measurement as the total flux in either filter inside the intersection of masks of the slit aperture and the Sunburst Arc, proceeding with the measured photometry in otherwise the same fashion as T. E. Rivera-Thorsen et al. (2019). See Table 3 for the results.

For each slit aperture and each filter, we estimated the uncertainty of each pixel in the images as the standard deviation of the flux densities outside of the arc mask but inside the aperture. We conservatively assumed a constant 10% uncertainty for the Starburst99 stellar continuum fits of each spectrum. We propagated these uncertainties through the calculation of the LyC escape fractions.

3.5. Measuring Ly α Properties

For all the following quantities, we used a Monte Carlo measurement process of 10,000 iterations with a burn-in simulation of 1000 iterations to estimate their values, in which we assumed the flux density and flux density uncertainty

Table 3
HST-based Properties of the MagE Spectra

Slit	F_{275}	F_{814}	$f_{\text{esc}}^{\text{LyC}}$
M5	20 ± 20	14580 ± 70	4 ± 5
M4	4 ± 20	26760 ± 60	0.5 ± 3
M6	50 ± 20	26700 ± 200	6 ± 3
M3	40 ± 20	26680 ± 60	5 ± 3
M0	290 ± 30	32580 ± 80	46 ± 4
M2	370 ± 30	39740 ± 80	30 ± 3
M7	120 ± 20	19680 ± 60	22 ± 4
M8	100 ± 30	12900 ± 70	20 ± 5
M9	150 ± 30	21220 ± 70	19 ± 3

Note. From left to right: slit label; flux in the HST/WFC3 F275W and HST/ACS F814W filters (10^{-19} erg s $^{-1}$ cm $^{-2}$); and $f_{\text{esc}}^{\text{LyC}}$ (%), all computed according to Section 3.4.

associated with each wavelength bin of the MagE spectra corresponded, respectively, to the mean and standard deviation of a Gaussian distribution. In each iteration, we drew a random sample from the Gaussian distributions corresponding to each wavelength bin to create a new mock spectrum that we then used to measure the discussed quantities. In the main text, figures, and tables, for a given measurement's distribution we cite the median M , and absolute differences between M and the 16th and 84th percentiles A and B , respectively, of the Monte Carlo simulation results as M_{-A}^{+B} .

In all Ly α profiles, we measured the FWHM of the central and redshifted Ly α peaks (Section 3.5.4), the ratio $f_{\text{min}}/f_{\text{cont}}$ (introduced in Section 3.5.5), the rest-frame Ly α equivalent width (EW; Section 3.5.1), and central escape fraction f_{cen} (R. P. Naidu et al. 2022; introduced later in Section 3.5.3). If the Ly α profile also had a blueshifted Ly α peak, we measured its FWHM and the velocity separation between the redshifted and blueshifted Ly α peaks (Section 3.5.4). In nonstacked spectra, we also measured the magnification-corrected Ly α luminosity (Section 3.5.2). Table 4 contains the measurements.

3.5.1. Equivalent Width

The EW of an absorption or emission line is a measure of its strength relative to the continuum level. In this work, we choose the convention that emission lines have positive EWs, and vice versa for absorption lines, so that the EW is

$$\text{EW} = - \int_{\lambda_1}^{\lambda_2} \left(1 - \frac{F_\lambda}{F_c} \right) d\lambda. \quad (1)$$

Here F_λ is the flux density, F_c the continuum flux density, and λ_1, λ_2 are the integration bounds over the spectral feature.

We applied Equation (1) to compute the rest-frame Ly α EW by integrating between 1212 and 1221 Å in the rest frame, as in H. Yang et al. (2017). We sampled the continuum flux density as the median flux density between 1221 and 1225 Å in the rest frame.

3.5.2. Luminosity

To compute the Ly α luminosity, we integrated the continuum-subtracted (taking the local continuum as in Section 3.5.1), magnification-corrected flux density between 1212 and 1221 Å in the rest frame.

Table 4
Ly α Measurements

Slit	v_{sep} (km s $^{-1}$)	FWHM (Blue) (km s $^{-1}$)	FWHM (Center) (km s $^{-1}$)	FWHM (Red) (km s $^{-1}$)	$f_{\text{min}}/f_{\text{cont}}$	EW (Å)	f_{cen} (%)	Luminosity (10 41 erg s $^{-1}$)
NL	79 $^{+7}_{-9}$	280 $^{+9}_{-9}$	2.0 $^{+0.3}_{-0.3}$	7.9 $^{+0.4}_{-0.4}$	10.4 $^{+0.2}_{-0.2}$...
L	331 $^{+3}_{-3}$	202 $^{+4}_{-5}$	79 $^{+3}_{-3}$	261 $^{+9}_{-6}$	16.9 $^{+0.3}_{-0.4}$	25.5 $^{+0.6}_{-0.6}$	26.7 $^{+0.1}_{-0.1}$...
M5	$\lesssim 70$	256 $^{+9}_{-10}$	0.7 $^{+0.3}_{-0.2}$	4.4 $^{+0.5}_{-0.5}$	7.4 $^{+0.3}_{-0.3}$	2.9 $^{+0.2}_{-0.2}$
M4	$\lesssim 80$	240 $^{+9}_{-8}$	2.5 $^{+0.2}_{-0.2}$	7.4 $^{+0.7}_{-0.7}$	11.7 $^{+0.4}_{-0.4}$	12.4 $^{+0.7}_{-0.7}$
M6	88 $^{+6}_{-9}$	236 $^{+9}_{-5}$	5.8 $^{+0.2}_{-0.3}$	11.9 $^{+0.7}_{-0.7}$	10.0 $^{+0.2}_{-0.2}$	2.57 $^{+0.08}_{-0.08}$
M3	302 $^{+6}_{-7}$	180 $^{+10}_{-10}$	83 $^{+7}_{-7}$	230 $^{+7}_{-6}$	11.5 $^{+0.4}_{-0.5}$	24 $^{+1}_{-1}$	24.5 $^{+0.2}_{-0.2}$	14.5 $^{+0.3}_{-0.3}$
M0	355 $^{+4}_{-4}$	175 $^{+6}_{-5}$	89 $^{+3}_{-3}$	244 $^{+4}_{-4}$	15.7 $^{+0.3}_{-0.3}$	23.5 $^{+0.8}_{-0.7}$	19.8 $^{+0.1}_{-0.1}$	1120 $^{+10a}_{-10}$
M2	342 $^{+8}_{-10}$	180 $^{+10}_{-10}$	70 $^{+7}_{-5}$	250 $^{+20}_{-20}$	18.3 $^{+0.7}_{-0.8}$	23 $^{+1}_{-1}$	25.6 $^{+0.2}_{-0.2}$	24.9 $^{+0.4}_{-0.4}$
M7	313 $^{+4}_{-4}$	202 $^{+6}_{-5}$	76 $^{+3}_{-3}$	244 $^{+4}_{-4}$	17.1 $^{+0.3}_{-0.3}$	25.6 $^{+0.7}_{-0.7}$	29.8 $^{+0.2}_{-0.2}$	25.4 $^{+0.2}_{-0.2}$
M8	326 $^{+4}_{-4}$	196 $^{+7}_{-7}$	80 $^{+4}_{-5}$	258 $^{+9}_{-5}$	18.6 $^{+0.5}_{-0.5}$	29 $^{+1}_{-1}$	21.4 $^{+0.1}_{-0.1}$	31.5 $^{+0.3}_{-0.3}$
M9	328 $^{+7}_{-7}$	200 $^{+10}_{-10}$	85 $^{+4}_{-4}$	255 $^{+6}_{-6}$	14.5 $^{+0.5}_{-0.5}$	25 $^{+2}_{-1}$	26.4 $^{+0.2}_{-0.3}$	18.1 $^{+0.3}_{-0.3}$

Notes. From left to right: slit label; peak separation between the redshifted and blueshifted Ly α peaks (in kilometers per second); FWHM of the blueshifted, central, and redshifted Ly α peaks (in kilometers per second), respectively; ratio between the “minimum” flux density between the redshifted and blueshifted Ly α peaks and the local continuum flux density; rest-frame Ly α equivalent width (in angstroms); central escape fraction (%); and magnification-corrected Ly α luminosity (10 41 erg s $^{-1}$). Because the deconvolved FWHMs of the central Ly α peaks of slits M4 and M5 were not significantly greater than the instrumental line-spread function FWHM (~ 55 km s $^{-1}$), we quote the 84th percentiles of those measurements as an upper bound on the intrinsic FWHM of their central Ly α peaks.

^a Slit M0’s observation was taken through thin cloud cover that prevented an accurate fluxing, so its significantly larger luminosity is not an accurate estimate. We do not include this data point in any figures or when estimating any correlations involving the Ly α luminosity. See Table 1 for more information about the observation.

3.5.3. f_{cen}

The central fraction of Ly α flux, f_{cen} , introduced by R. P. Naidu et al. (2022), is

$$f_{\text{cen}} = \frac{\text{Ly}\alpha \text{ flux between } \pm 100 \text{ km s}^{-1}}{\text{Ly}\alpha \text{ flux between } \pm 1000 \text{ km s}^{-1}}, \quad (2)$$

so named because it integrates the flux densities in the specified velocity bands centered on the wavelength of Ly α . The numerator, which targets a narrow band about the Ly α wavelength, is sensitive to Ly α photons that have not been rescattered (attenuated) much by HI (dust). But due to the “random walk” nature of a Ly α photon’s radiative transfer, the numerator also includes any Ly α photons that randomly walk back to the central wavelength band after significant reprocessing. If significantly underdense sight lines exist to the areas of Ly α production, Ly α photons escaping through them should appear in the central wavelength band. The denominator captures virtually all Ly α flux. Thus, f_{cen} represents the relative strength of minimally scattered Ly α photons compared to the total number of Ly α photons. R. P. Naidu et al. (2022) predict that f_{cen} should correlate with the LyC escape fraction, since LyC photons must navigate similar obstacles (i.e., HI and dust) to escape a galaxy.

3.5.4. Peak Widths and Separation

Determining the width and separation of the Ly α peaks depends on the structure of the Ly α profile in question. We organized the spectra into two cases: (i) there is a redshifted, blueshifted, and central Ly α peak, and (ii) there is not a clear blueshifted Ly α peak. This dichotomy implies that all the spectra have central Ly α peaks, even though slit M5 does not clearly show a central Ly α peak. We still include slit M5 in the two-case dichotomy (the latter case) in order to constrain the

possibility of a faint, unresolved central Ly α peak. Most (all the LyC-leaking spectra and slit M3) of the spectra fall into case (i), and only some of the non-LyC-leaking spectra occupy case (ii) (slits M4, M5, and M6).

T. E. Rivera-Thorsen et al. (2017) previously modeled the central peak as a Gaussian function of the form

$$\Gamma_{\lambda}(v) = \alpha e^{-\frac{1}{2}(v-\mu)/\sigma)^2}, \quad (3)$$

where α is its amplitude, μ its centroid, and σ its standard deviation. Other authors (e.g., R. P. Mallery et al. 2012; V. U et al. 2015; X. Cao et al. 2020) have treated double-peaked Ly α profiles (those with a redshifted and blueshifted Ly α peak) as two skewed Gaussian functions that follow the form

$$\xi_{\lambda}(v) = \Gamma_{\lambda}(v) \left[1 + \text{erf} \left(\frac{\omega(v-\mu)}{\sqrt{2}\sigma} \right) \right]. \quad (4)$$

Here ω is the skewness, which controls how skewed the distribution is, and $\text{erf}(x)$ is the error function, a complex function with complex variable x defined as

$$\text{erf}(x) = \frac{2}{\sqrt{\pi}} \int_0^x e^{-t^2} dt. \quad (5)$$

Right-skewed distributions (i.e., a redshifted Ly α peak) have $\omega > 0$ and left-skewed distributions (i.e., a blueshifted Ly α peak) have $\omega < 0$.

We combined these two approaches by simultaneously fitting the Ly α profiles to a combination of Gaussian and skewed Gaussian functions with the `curve_fit()` function in the SciPy Python package. We directly measured each peak’s FWHM and the separation between the redshifted and blueshifted Ly α peaks v_{sep} from the resulting fit. To determine the intrinsic FWHM of a peak, we assumed the overall FWHM measured from the observed spectrum as Gaussian, and deconvolved it with the assumed Gaussian line-spread function of the instrument ($\text{FWHM} = c/R$), randomly sampling the

spectral resolution at each iteration of the Monte Carlo procedure from a Gaussian distribution described by the spectral resolutions in Table 1. We determined the spectral resolution of the stacked spectra by averaging the spectral resolutions of their composite spectra and adding the associated uncertainties in quadrature. The resulting FWHM is what we report in Table 4. We fitted the following functions for the two aforementioned cases:

$$(i) \xi_{\lambda}^{\text{blue}} + \xi_{\lambda}^{\text{red}} + \Gamma_{\lambda} + c,$$

$$(ii) \xi_{\lambda}^{\text{red}} + \Gamma_{\lambda} + c,$$

where c is a scalar continuum contribution. In case (ii), even when there is not a clear central Ly α peak resolved from the redshifted Ly α peak, attempting to fit a central Gaussian component can directly constrain the strength of any unresolved central Ly α peak. The stacked spectrum of the non-LyC-leaking apertures is strongly suggestive of such an instance, since it shows a noticeable bulge on the blueward side of the redshifted Ly α peak poorly reproduced by a single skewed Gaussian (Figure 3). The best-fit model parameters appear in Table 7.

3.5.5. f_{\min}/f_{cont}

Instead of a triple-peaked profile, Ly α profiles are almost always single or double peaked, showing some combination of a redshifted and blueshifted Ly α peak, but no clear, central Ly α peak of directly escaping Ly α photons. In this case, a common parameter closely connected to the HI scattering environment is the ratio between the minimum flux density between the redshifted and blueshifted Ly α peaks, f_{\min} , and the flux density of the local continuum, f_{cont} (e.g., A. E. Jaskot et al. 2019). Functionally, this quantity directly constrains the strength of a central peak of direct-escape Ly α photons. Usually, such a peak (if it exists) is completely unresolved due to much stronger, nearby redshifted and blueshifted Ly α peaks. Clearly, this is not the case in the Sunburst Arc, so this measurement breaks down, as often the peak Ly α intensity appears between the redshifted and blueshifted Ly α peaks (Figures 2 and 3).

Instead, we measured the central Ly α peak’s fitted amplitude as f_{\min} , as this interpretation captures the “spirit” of f_{\min}/f_{cont} , to gauge the prevalence of direct-escape Ly α photons (which constitute the central Ly α peak) and probe the HI column density. We took f_{cont} as the local continuum flux density fitted in the functions described in Section 3.5.4.

4. Results

Previous work has investigated a wide range of correlations between Ly α and LyC parameters, which is critical to understand the intimate relation between Ly α and LyC escape. Observations have found positive correlations between the following:

1. $f_{\text{esc}}^{\text{LyC}} - \text{Ly}\alpha \text{ EW}$ (A. Verhamme et al. 2017; T. J. Fletcher et al. 2019; S. R. Flury et al. 2022b; A. Saldana-Lopez et al. 2022; A. J. Pahl et al. 2023);
2. $f_{\text{esc}}^{\text{LyC}} - \text{Ly}\alpha \text{ FWHM}$ (I. G. Kramarenko et al. 2024);
3. $f_{\text{esc}}^{\text{LyC}} - f_{\text{cen}}$ (R. P. Naidu et al. 2022);
4. $f_{\text{esc}}^{\text{LyC}} - f_{\min}/f_{\text{cont}}$ (S. Gazagnes et al. 2020);
5. $v_{\text{sep}} - \text{Ly}\alpha \text{ FWHM}$ (A. Verhamme et al. 2018; J. Kerutt et al. 2022); and

6. $f_{\min}/f_{\text{cont}} - \text{Ly}\alpha \text{ EW}$ (A. E. Jaskot et al. 2019).

Negative correlations have been found between the following:

1. $f_{\text{esc}}^{\text{LyC}} - v_{\text{sep}}$ (A. Verhamme et al. 2017; Y. I. Izotov et al. 2018c, 2021c, 2022; S. Gazagnes et al. 2020; S. R. Flury et al. 2022b; R. P. Naidu et al. 2022);
2. $f_{\min}/f_{\text{cont}} - v_{\text{sep}}$ (A. E. Jaskot et al. 2019);
3. $v_{\text{sep}} - \text{Ly}\alpha \text{ EW}$ (A. Verhamme et al. 2017; A. E. Jaskot et al. 2019; R. Marques-Chaves et al. 2020); and
4. $\text{Ly}\alpha \text{ FWHM} - \text{Ly}\alpha \text{ EW}$ (T. Hashimoto et al. 2017).

And noncorrelations between the following:

1. $f_{\text{esc}}^{\text{LyC}} - \text{Ly}\alpha \text{ EW}$ (U. Mestric et al. 2020);
2. $v_{\text{sep}} - \text{Ly}\alpha \text{ EW}$ (J. Kerutt et al. 2022); and
3. $\text{Ly}\alpha \text{ FWHM} - \text{Ly}\alpha \text{ EW}$ (J. Kerutt et al. 2022).

Additionally, simulations have made predictions about correlations between some of the aforementioned quantities, including positive correlations between the following:

1. $f_{\text{esc}}^{\text{LyC}} - \text{Ly}\alpha \text{ luminosity}$ (T. Kimm et al. 2022; M. Maji et al. 2022); and
2. $v_{\text{sep}} - \text{Ly}\alpha \text{ FWHM}$ (A. Verhamme et al. 2015).

And negative correlations between the following:

1. $f_{\text{esc}}^{\text{LyC}} - v_{\text{sep}}$ (A. Verhamme et al. 2015; M. Dijkstra et al. 2016; K. Kakiichi & M. Gronke 2021; T. Kimm et al. 2022); and
2. $v_{\text{sep}} - \text{Ly}\alpha \text{ EW}$ (A. Verhamme et al. 2015).

To compare our results with previous work, we measured the Pearson correlation coefficient r and type “b” Kendall rank correlation coefficient τ between all combinations among the Ly α parameters and $f_{\text{esc}}^{\text{LyC}}$ for each iteration of the Monte Carlo simulation (Table 5). We incorporated uncertainty in $f_{\text{esc}}^{\text{LyC}}$ into the measurement of correlations for each iteration by randomly sampling $f_{\text{esc}}^{\text{LyC}}$ according to a Gaussian distribution, where the reported value and uncertainty listed in Table 3 correspond to the mean and standard deviation. We found $f_{\text{esc}}^{\text{LyC}}$ to be strongly correlated with the Ly α parameters v_{sep} , f_{\min}/f_{cont} , and Ly α EW, and anticorrelated with the blueshifted Ly α peak FWHM (Table 5). Between Ly α parameters, we found the following strong correlations:

1. $\text{Ly}\alpha \text{ EW} - f_{\min}/f_{\text{cont}}$;
2. $f_{\text{cen}} - f_{\min}/f_{\text{cont}}$;
3. $f_{\text{cen}} - \text{Ly}\alpha \text{ EW}$;
4. $\text{Ly}\alpha \text{ luminosity} - f_{\min}/f_{\text{cont}}$;
5. $\text{Ly}\alpha \text{ luminosity} - \text{Ly}\alpha \text{ EW}$; and
6. $\text{Ly}\alpha \text{ luminosity} - f_{\text{cen}}$ (Table 5).

We also found an anticorrelation between f_{cen} and v_{sep} . Apart from the correlation between $f_{\text{esc}}^{\text{LyC}}$ and v_{sep} , these correlations generally align with the previous works mentioned above.

Surprisingly, the Ly α peak separation v_{sep} and $f_{\text{esc}}^{\text{LyC}}$ show a very significant positive correlation ($r = 0.93_{-0.05}^{+0.03}$), contrary to the literature consensus of a negative correlation between the (galaxy-integrated) v_{sep} and $f_{\text{esc}}^{\text{LyC}}$. This unexpected result may be due to several factors. First, the peculiar shapes of some of the blueshifted Ly α peaks (namely slits M0, M2, and M9 in Figure 2, which appear slightly asymmetric relative to the fitted Ly α peak’s center) near their center may obfuscate the determination of an accurate Ly α peak separation since we have assumed their skewed Gaussianity (see Section 4.2 for

Table 5
Correlations between Ly α and LyC Parameters

	r	τ
FWHM (b) $-v_{\text{sep}}$	$-0.4_{-0.2}^{+0.2}$	$-0.2_{-0.2}^{+0.2}$
FWHM (c) $-v_{\text{sep}}$	$0.1_{-0.3}^{+0.4}$	$0.0_{-0.2}^{+0.3}$
FWHM (r) $-v_{\text{sep}}$	$0.4_{-0.2}^{+0.2}$	$0.3_{-0.2}^{+0.2}$
$f_{\text{min}}/f_{\text{cont}}-v_{\text{sep}}$	$0.4_{-0.2}^{+0.1}$	$0.1_{-0.1}^{+0.2}$
Ly α EW $-v_{\text{sep}}$	$-0.2_{-0.2}^{+0.2}$	$-0.1_{-0.2}^{+0.2}$
$f_{\text{cen}}-v_{\text{sep}}$	$-0.5_{-0.1}^{+0.1}$	$-0.3_{-0.1}^{+0.1}$
Ly α $L-v_{\text{sep}}$	$0.4_{-0.2}^{+0.2}$	$0.2_{-0.2}^{+0.2}$
$f_{\text{esc}}^{\text{LyC}}-v_{\text{sep}}$	$0.93_{-0.05}^{+0.03}$	$0.7_{-0.1}^{+0.1}$
FWHM (c) $-FWHM$ (b)	$-0.3_{-0.3}^{+0.3}$	$-0.2_{-0.2}^{+0.3}$
FWHM (r) $-FWHM$ (b)	$0.5_{-0.4}^{+0.2}$	$0.3_{-0.3}^{+0.2}$
$f_{\text{min}}/f_{\text{cont}}-FWHM$ (b)	$0.1_{-0.3}^{+0.3}$	$0.0_{-0.2}^{+0.2}$
Ly α EW $-FWHM$ (b)	$0.5_{-0.2}^{+0.2}$	$0.4_{-0.2}^{+0.2}$
$f_{\text{cen}}-FWHM$ (b)	$0.5_{-0.2}^{+0.2}$	$0.4_{-0.2}^{+0.2}$
Ly α $L-FWHM$ (b)	$0.2_{-0.3}^{+0.3}$	$0.2_{-0.2}^{+0.4}$
$f_{\text{esc}}^{\text{LyC}}-FWHM$ (b)	$-0.71_{-0.06}^{+0.08}$	$-0.5_{-0.1}^{+0.1}$
FWHM (r) $-FWHM$ (c)	$-0.2_{-0.2}^{+0.2}$	$-0.2_{-0.2}^{+0.2}$
$f_{\text{min}}/f_{\text{cont}}-FWHM$ (c)	$0.4_{-0.2}^{+0.2}$	$0.1_{-0.2}^{+0.1}$
Ly α EW $-FWHM$ (c)	$0.5_{-0.2}^{+0.2}$	$0.2_{-0.2}^{+0.2}$
$f_{\text{cen}}-FWHM$ (c)	$0.3_{-0.2}^{+0.2}$	$0.1_{-0.2}^{+0.1}$
Ly α $L-FWHM$ (c)	$0.2_{-0.2}^{+0.2}$	$0.1_{-0.2}^{+0.1}$
$f_{\text{esc}}^{\text{LyC}}-FWHM$ (c)	$0.51_{-0.08}^{+0.08}$	$0.28_{-0.1}^{+0.06}$
$f_{\text{min}}/f_{\text{cont}}-FWHM$ (r)	$-0.1_{-0.2}^{+0.2}$	$0.1_{-0.1}^{+0.1}$
Ly α EW $-FWHM$ (r)	$-0.1_{-0.2}^{+0.2}$	$0.1_{-0.1}^{+0.1}$
$f_{\text{cen}}-FWHM$ (r)	$-0.1_{-0.2}^{+0.2}$	$0.0_{-0.1}^{+0.1}$
Ly α $L-FWHM$ (r)	$0.3_{-0.3}^{+0.2}$	$0.3_{-0.2}^{+0.1}$
$f_{\text{esc}}^{\text{LyC}}-FWHM$ (r)	$0.18_{-0.09}^{+0.09}$	$0.28_{-0.1}^{+0.06}$
Ly α EW $-f_{\text{min}}/f_{\text{cont}}$	$0.965_{-0.01}^{+0.009}$	$0.71_{-0.07}^{+0.07}$
$f_{\text{cen}}-f_{\text{min}}/f_{\text{cont}}$	$0.898_{-0.009}^{+0.009}$	$0.56_{-0.04}^{+0.04}$
Ly α $L-f_{\text{min}}/f_{\text{cont}}$	$0.90_{-0.01}^{+0.01}$	$0.79_{-0.07}^{+0.07}$
$f_{\text{esc}}^{\text{LyC}}-f_{\text{min}}/f_{\text{cont}}$	$0.74_{-0.07}^{+0.06}$	$0.61_{-0.06}^{+0.1}$
$f_{\text{cen}}-Ly\alpha$ EW	$0.91_{-0.01}^{+0.01}$	$0.60_{-0.07}^{+0.04}$
Ly α $L-Ly\alpha$ EW	$0.85_{-0.02}^{+0.02}$	$0.71_{-0.07}^{+0.07}$
$f_{\text{esc}}^{\text{LyC}}-Ly\alpha$ EW	$0.60_{-0.08}^{+0.07}$	$0.3_{-0.1}^{+0.1}$
Ly α $L-f_{\text{cen}}$	$0.79_{-0.01}^{+0.01}$	$0.6_{-0.1}^{+0.1}$
$f_{\text{esc}}^{\text{LyC}}-f_{\text{cen}}$	$0.50_{-0.08}^{+0.07}$	$0.33_{-0.1}^{+0.06}$
$f_{\text{esc}}^{\text{LyC}}-Ly\alpha$ L	$0.50_{-0.07}^{+0.07}$	$0.33_{-0.1}^{+0.06}$

Note. Statistical correlations between the Ly α parameters and $f_{\text{esc}}^{\text{LyC}}$. From left to right: the parameter pair; the Pearson correlation coefficient r ; and the type “b” Kendall rank correlation coefficient τ . The minimal number of data points (no more than 11 for any pair of parameters) means there are not many unique values of τ , which causes many of the listed values and uncertainties to be similar, or in extreme cases for high-SNR parameter measurements, for the 16th and 84th percentiles listed to be the same value as the median.

more discussion). Furthermore, the dynamic range of v_{sep} measured from the spectra is minimal, and slit M3 impacts the correlation as a clear outlier to the other data points (Figure 6). The resolutions of the spectra ($R \gtrsim 5000$) are sufficiently high that they may be beginning to resolve departures from the skewed Gaussianity assumption, and thus also the simple shell model geometry and kinematics typically invoked to explain double-peaked Ly α emitters (LAEs). Furthermore, because the spectra target small source-plane areas, they should be more sensitive to any local departures from an idealized shell model. Also, the established $v_{\text{sep}} - f_{\text{esc}}^{\text{LyC}}$ anticorrelation paradigm has mostly been built from double-peaked LAEs that suggest a

much different mode for LyC escape—where LyC photons may escape because the optical depth of H I is sufficiently low that many LyC photons do not interact with the H I. This is not the dominant mode of LyC escape in the Sunburst Arc, where LyC photons primarily escape through an extremely underdense, thin channel (T. E. Rivera-Thorsen et al. 2017; K. J. Kim et al. 2023).

We found some moderate correlations and a strong anticorrelation among the measurement pairs including the FWHM of a Ly α peak, but no strong correlations (Table 5). We measured very similar FWHMs for all the redshifted and central Ly α peaks (excluding slits M4 and M5 in the latter, which had central Ly α peak FWHMs not much larger than the instrumental dispersion FWHM of $\sim 55 \text{ km s}^{-1}$; Table 4). The width of a Ly α peak should be sensitive to the number of scattering events the signal experiences before escaping the galaxy, but we found no clear correlations between the Ly α peak FWHM and other proxies for the H I scattering environment. However, the FWHM measurements suffer from fewer data points (indicating where a certain Ly α peak is not present in a profile). Additionally, there is little dynamic range in any of the FWHMs, which fundamentally limits the data’s sensitivity to any correlations between FWHMs and other quantities.

The strength of all the measured correlations are subject to caveats. In total, the spectra only target $\lesssim 10$ distinct regions in the galaxy’s source plane (Figure 7). Of those regions, the LyC-leaking apertures capture one region, and the non-LyC-leaking apertures capture the remaining regions. But based upon the source-plane reconstruction (Figure 7), the non-LyC-leaking apertures (perhaps excluding slit M6 based upon its geometry) could each include significant contributions from multiple regions of the galaxy. This complicates the interpretation of their Ly α properties since the light in the apertures are the sum of multiple galaxy environments. Also, the LyC-leaking apertures dominate the sample size of many of the parameters and tend to cluster together since they target the same source-plane object. This means slit M3, often an outlier to the LyC-leaking region’s sample despite also showing a triple-peaked Ly α profile (Figure 6), can greatly impact the apparent relation between two measurements.

Additionally, with enough measurements compared against each other, spurious correlations are virtually certain (dubbed data dredging, data snooping, or p -hacking). We made 36 comparisons between nine measurements, with few data points (5–11 for any given comparison), so we cannot entirely discount a false detection of a correlation at the measured uncertainties.

4.1. $f_{\text{esc}}^{\text{LyC}}$

We found higher $f_{\text{esc}}^{\text{LyC}}$ in the MagE apertures targeting images T. E. Rivera-Thorsen et al. (2019) identified as LyC leakers ($\gtrsim 20\%$) than those targeting non-LyC-leaking images ($\lesssim 5\%$; Table 3). Despite the larger aperture size and PSF of the MagE observations compared to the data and methodology of T. E. Rivera-Thorsen et al. (2019), the $f_{\text{esc}}^{\text{LyC}}$ of the LyC-leaking apertures are comparable to or only slightly lower than what T. E. Rivera-Thorsen et al. (2019) reported. For comparison, T. E. Rivera-Thorsen et al. (2019) reported a median absolute, IGM absorption-corrected LyC escape fraction from their apertures on the LyC-leaking region of $\approx 32\%$. Table 3 summarizes the measured HST photometry and $f_{\text{esc}}^{\text{LyC}}$.

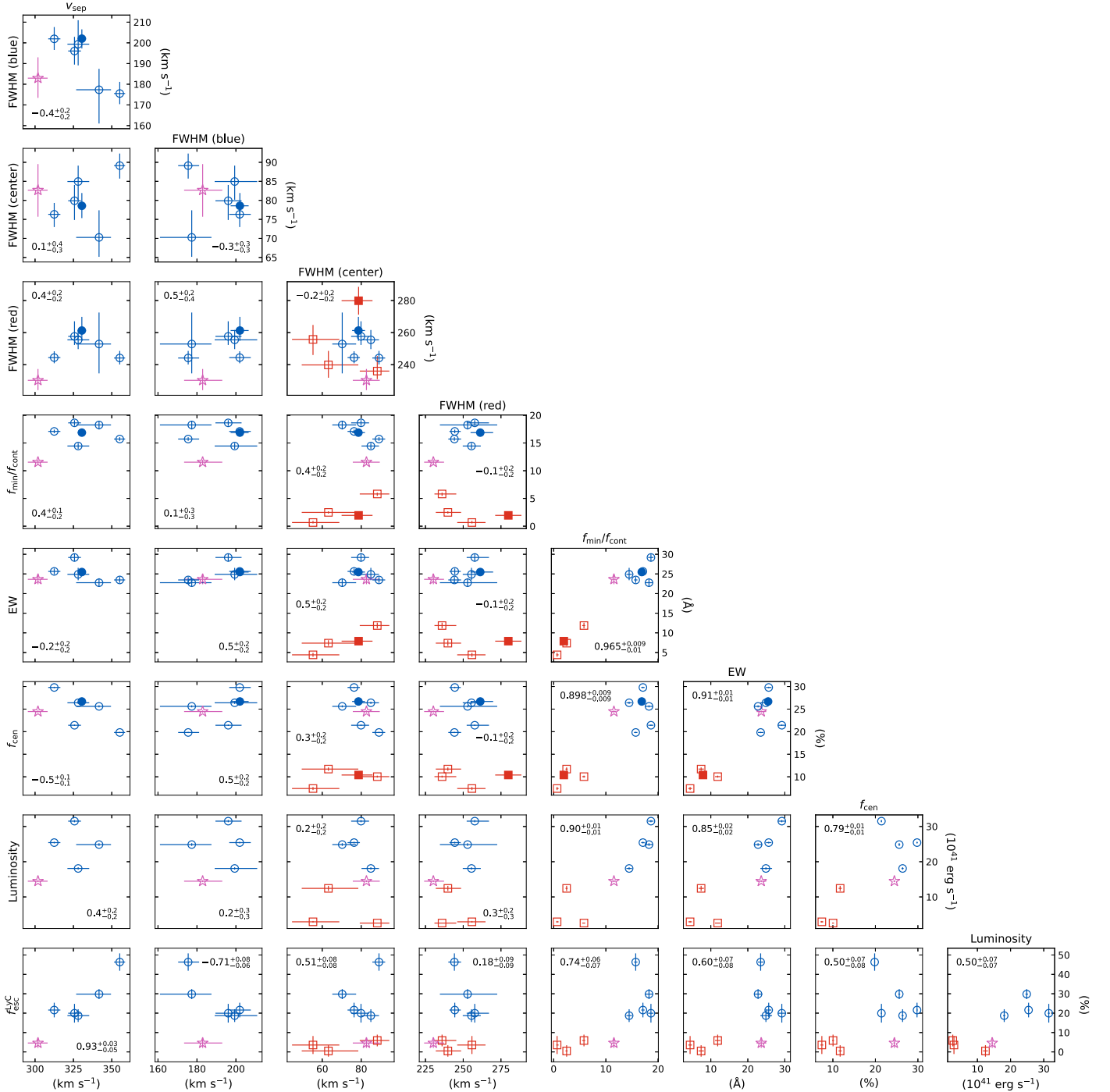


Figure 6. Corner plot of the Ly α measurements, as well as $f_{\text{esc}}^{\text{LyC}}$. Red squares are non-LyC-leaking apertures, blue circles are LyC-leaking apertures, and the pink star is slit M3. Filled markers are the stacked spectra. The value annotated in each plot indicates the Pearson correlation coefficient between the two quantities. Table 5 also lists the Pearson correlation coefficients and type “b” Kendall rank correlation coefficients.

As expected, the non-LyC-leaking apertures show no obvious LyC emission in the F275W image (Figure 4) and minimal $f_{\text{esc}}^{\text{LyC}}$ in our measurements, which use deeper rest-LyC imaging than T. E. Rivera-Thorsen et al. (2019; 5413 s versus 86,902 s). The F275W image of the LyC-leaking images reveals that the LyC emission is extremely compact (Figure 4), and at the resolution of HST, the non-LyC-leaking slit apertures do not cover any images of the LyC leaker. Due to the convolution of the data with the ground-based seeing conditions (Section 3.4), some non-LyC-leaking images may have smaller $f_{\text{esc}}^{\text{LyC}}$ than suggested by this work’s aperture-based

measurements because the simulation can cause LyC flux from nearby LyC-leaking images to enter the aperture. Since so little LyC flux should already be in a non-LyC-leaking aperture before the convolution, even a small amount could cause a large proportional change, but this likely only affects slit M3, and to a lesser extent slit M4, due to their proximity to images of the LyC-leaking region (Figure 1).

The LyC-leaking apertures show similar or slightly lower $f_{\text{esc}}^{\text{LyC}}$ than the corresponding median absolute, IGM absorption-corrected LyC escape fraction measurement in T. E. Rivera-Thorsen et al. (2019). We suggest two factors

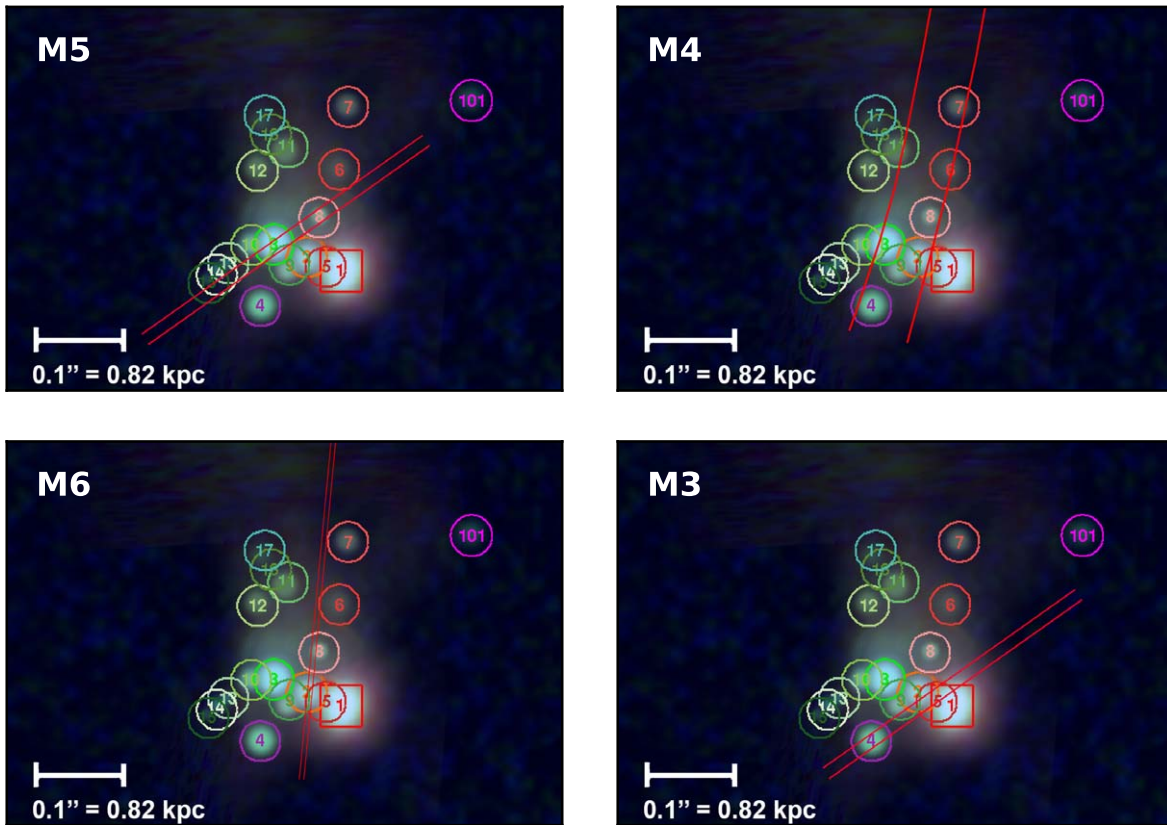


Figure 7. A portion of the approximate source-plane reconstruction of the Sunburst Arc from K. Sharon et al. (2022) with ray-traced non-LyC-leaking apertures overlaid in red and labeled in the top left of each panel. The numbered circles and square correspond to the unique source-plane regions identified in K. Sharon et al. (2022). Region 1 boxed in red is the LyC leaker.

that may cause this reduction. First, the $f_{\text{esc}}^{\text{LyC}}$ calculation is inversely proportional to the F814W flux. Since our aperture—in effect of order $\sim 0''.85$ (slit width) $\times 1''.7$ (radial arc width)—is much larger than what T. E. Rivera-Thorsen et al. (2019) used ($\sim 0''.12 \times 0''.12$), it is more sensitive to the F814W emission, which is more extended than the compact LyC emission in F275W. This means the F814W flux can effectively dilute the $f_{\text{esc}}^{\text{LyC}}$. Second, the convolution of the data with the ground-based seeing conditions (Section 3.4) introduces an artificial aperture loss. Some LyC flux leaves an aperture due to the PSF of the ground-based seeing conditions, decreasing $f_{\text{esc}}^{\text{LyC}}$. This affects the LyC-leaking apertures more significantly due to the comparably sized slit width and PSF. A possible exception is slit M2 (and slit M8 less so), where the slit placement’s immediate proximity to the LyC-leaking image 1.9 (Figure 1) suggests nontrivial LyC flux from image 1.9 enters its aperture, even though slit M2 does not directly cover it. This is reflected in slit M2’s $f_{\text{esc}}^{\text{LyC}}$, second in strength only to slit M0. A similar process may happen in slit M0 as LyC flux from image 1.6 of the LyC-leaking region enters the aperture. Slit M0 may have an exceptionally high LyC escape fraction because it covers two images of the LyC-leaking region—slit M0’s $f_{\text{esc}}^{\text{LyC}}$ is also roughly double the LyC escape fractions of the other LyC-leaking apertures.

4.2. Ly α Properties

Our Ly α fitting (Section 3.5.4) well replicates the overall structure of each velocity profile (Figures 2 and 3), but there are some residuals. Deviations from Gaussian or skewed Gaussian behavior are noticeable at the high spectral resolution and high

SNR of the spectra, and likely reflect the fact that the outflowing H I gas has a much more complex geometry than the assumed isotropic shell used to justify the ad hoc Gaussian and skewed Gaussian model. Key differences include the following:

1. There is some excess flux in the red tails of the profiles not captured by the fits (Figures 2 and 3). These features might reflect velocity intervals in the outflowing gas that have slightly higher column densities.
2. The skewed Gaussian model fits to the Ly α peaks are not able to fully reproduce the shapes of the spectra. The strongest residual appears in slit M8’s redshifted Ly α peak fit (Figure 2), in which the data exhibit a sharper decline than the fit can produce. The impact of this effect on the line profile measurements is primarily an additional, small systematic error in the fitted FWHMs, biasing them slightly high.
3. The centers of the redshifted Ly α peaks are often broader than the fits. This is especially clear in slits M6, M7, M8, and M9 (Figure 2). The minor emission peaks reported by E. Solhaug et al. (2024) at $\approx 130 \text{ km s}^{-1}$ in high-resolution MIKE spectra (Figure 6 therein) may cause this, as the comparatively much lower resolution MagE spectra do not fully resolve these features.
4. An absorber centered at $\sim 400 \text{ km s}^{-1}$ attenuates the high-velocity tails of the blueshifted Ly α peaks, as also reported in E. Solhaug et al. (2024) with much higher resolution spectra. Additionally, the peak structure in several blueshifted Ly α peaks near their center seems

more complex than a modest number of Gaussian or skewed Gaussian components can reproduce (particularly slits M0, M2, and M9 in Figure 2).

We also note that the structure of the redshifted Ly α peak is remarkably consistent across all of the spectra, indicating that it is likely a “global” feature. The remainder of this section discusses the measurements of the individual Ly α parameters. Table 4 summarizes the results.

4.2.1. Equivalent Width

The Ly α EWs of the LyC-leaking apertures ($\sim 22\text{--}30\text{ \AA}$) are higher than those of the non-LyC-leaking apertures ($\sim 4\text{--}12\text{ \AA}$) by a factor of $\gtrsim 2$ (excepting slit M3; 24^{+1}_-1 \AA ; Table 4). Since Ly α photons primarily originate from H II regions, this strong difference is consistent with the much younger age of the LyC-leaking population ($3.3 \pm 0.5\text{ Myr}$ according to R. Mainali et al. 2022).

4.2.2. Luminosity

We found $\log_{10}(L_{\text{Ly}\alpha}[\text{erg s}^{-1}]) \sim 41.4 - 42.2$ in non-LyC-leaking apertures and $\sim 42.2\text{--}42.5$ in LyC-leaking apertures (Table 4). The relationship between Ly α and LyC flux is not always clear. In principle, they are at odds, since LyC photons absorbed by H I increase the supply of H II ions that can recombine and emit Ly α photons. But a large N_{HI} or dust content can effectively suppress both. The extinctions derived by R. Mainali et al. (2022) suggest the galaxy’s dust content does not vary significantly, indicating that older stellar populations in the non-LyC-leaking regions are the dominant effect causing the fainter Ly α luminosities.

4.2.3. f_{cen}

We found much higher f_{cen} in the LyC-leaking apertures ($\sim 20\%\text{--}30\%$) than non-LyC-leaking ones ($\sim 7\%\text{--}10\%$), except for slit M3 ($24.5^{+0.2}_{-0.2}\%$; Table 4). R. P. Naidu et al. (2022) previously measured $f_{\text{cen}} \approx 37\%$ for the LyC leaker in the Sunburst Arc with archival X-shooter data, though the area used to extract the spectrum in that work is unclear. E. Solhaug et al. (2024) also measured comparatively elevated f_{cen} with high-resolution MIKE spectra, finding $f_{\text{cen}} \approx 42\%$ for the LyC-leaking region and $f_{\text{cen}} \approx 37\%$ for approximately the same pointing as slit M3, which we judged to likely be a consequence of the much higher spectral resolution of their data ($R \approx 29,000$).

4.2.4. Peak Widths and Separation

Interestingly, the central and redshifted Ly α peak FWHMs are remarkably similar across most spectra (Table 4). The central Ly α peak FWHMs ($\sim 70\text{--}90\text{ km s}^{-1}$) are also consistent with the results of E. Solhaug et al. (2024), who measured central Ly α peak FWHMs of $\sim 71\text{--}95\text{ km s}^{-1}$ with the high-resolution ($R \approx 29,000$) Magellan/MIKE spectrograph for apertures approximately corresponding to slits M2, M3, and M0. The redshifted Ly α peak FWHMs are $\sim 230\text{--}250\text{ km s}^{-1}$, without significant difference between the LyC-leaking and non-LyC-leaking apertures. Some non-LyC-leaking spectra (specifically slits M3, M4, and M6) might have slightly narrower redshifted Ly α peaks than the LyC-leaking spectra, but the uncertainties make this unclear. If the difference is real, it conflicts with the expectation that the

thicker H I column densities suspected to exist in the non-LyC-leaking regions should broaden emerging Ly α peaks and attenuate LyC flux. However, because the spectra (1) probe small distances in the source plane (much smaller than the galaxy-wide scales of most Ly α observations), and (2) show highly unique Ly α profiles indicative of much different H I geometry and kinematics than often observed, the same intuitions may not hold in this exotic object. The notable exception is the stacked spectrum of the non-LyC-leaking apertures, which has the broadest redshifted Ly α peak FWHM ($280^{+9}_{-9}\text{ km s}^{-1}$). This may be connected to possible degeneracies in the model fitting, since the central Ly α peak in the stacked spectrum of the non-LyC-leaking apertures is much fainter than the redshifted Ly α peak.

The blueshifted Ly α peak FWHMs are not so unusually behaved, but we may detect true differences between them (e.g., slit M0 versus slit M7) due to the larger scatter (Table 4). If genuine, it is unclear if these differences could be attributable to differential magnification of the images, the viewing angle into the LyC-leaking region, or other effects.

We measured Ly α peak separations $\sim 300\text{--}350\text{ km s}^{-1}$ in the LyC-leaking apertures and the non-LyC-leaking aperture slit M3 with a triple-peaked Ly α profile (Table 4). Low-redshift calibrations compiled by Y. I. Izotov et al. (2022) suggest $f_{\text{esc}}^{\text{LyC}} \lesssim 10\%$ based upon these peak separations, much lower than the $f_{\text{esc}}^{\text{LyC}} \gtrsim 20\%$ we measured for the LyC-leaking apertures (Table 3). The exception is slit M3, which, despite its narrow peak separation ($302^{+6}_{-7}\text{ km s}^{-1}$), has a small LyC escape fraction ($f_{\text{esc}}^{\text{LyC}} = 5\% \pm 3\%$). As noted in Section 4.1, this may be an overestimate due to the simulated seeing effects (Section 3.4), as an image of the LyC-leaking region is near ($< 1''$) the slit M3 aperture (Figure 1).

4.2.5. $f_{\text{min}}/f_{\text{cont}}$

We measured $f_{\text{min}}/f_{\text{cont}} \sim 14 - 19$ in the LyC-leaking spectra, similar to Green Pea galaxies (GPs) with the narrowest Ly α peak separations (A. E. Jaskot et al. 2019). In the non-LyC-leaking spectra, excluding slit M3 ($f_{\text{min}}/f_{\text{cont}} = 11.5^{+0.4}_{-0.5}$), we found $f_{\text{min}}/f_{\text{cont}} \sim 1 - 6$, comparable to many GPs with wider peak separations (A. E. Jaskot et al. 2019). However, the driving cause of the $f_{\text{min}}/f_{\text{cont}}$ measured here is a directly escaping, separate Ly α peak. In most other works the measured f_{min} is consistent with two superimposed Ly α peaks expected from an isotropically expanding H I shell. This geometry is not representative of the Sunburst Arc since the central Ly α peak suggests a highly anisotropic ISM.

5. Discussion

A key piece in connecting Ly α and LyC escape in the Sunburst Arc is to explain the variety of Ly α profiles, especially the non-LyC-leaking apertures that show a triple-peaked Ly α profile or a central and redshifted Ly α peak. The essential picture explaining the triple-peaked Ly α profile observed in the images of the LyC leaker is well understood. T. E. Rivera-Thorsen et al. (2017) posited an ionized channel in a surrounding H I shell as the most likely mechanism to observe a triple-peaked structure. The much larger f_{cen} , $f_{\text{esc}}^{\text{LyC}}$, and Ly α escape fraction (K. J. Kim et al. 2023), and exceptionally blue UV slope (K. J. Kim et al. 2023) of the LyC-leaking region supports the existence of such a channel oriented along the sight line to the LyC-leaking region. The

young age of the LyC leaker suggested by stellar population fitting, in tandem with its strong UV stellar feedback features (e.g., the N V 1238, 1242 Å, C IV 1548, 1550 Å doublets with P-Cygni wind profiles shown in R. Mainali et al. 2022) and compact size ($r_{\text{eff}} \lesssim 32$ pc; K. Sharon et al. 2022) indicate an obvious culprit, with the strong LyC flux and outflows suited to puncture the surrounding H I medium and leak LyC photons.

What remains unclear are the mechanisms leading to the observed non-LyC-leaking Ly α profiles, since multiple show a central Ly α peak (slits M4, M6, and M3), and, in the case of slit M3, a triple-peaked Ly α profile (Figure 2). In the channel-escape hypothesis these are both associated with the presence of a LyC source, which does not appear in these apertures (Figure 4).

We have considered if differential magnification effects due to gravitational lensing could explain the observed non-LyC-leaking Ly α profiles. This scenario would require a high magnification gradient, which often occurs close to the critical curve (i.e., Figures 5 and 6 in K. Sharon et al. 2022), and can increase or decrease the weighting of the different physical regions within a lensed galaxy in the spectra that we observe. However, a simple analysis using the lens model (K. Sharon et al. 2022) rejects this as a plausible explanation for the spatially variable Ly α and LyC properties of the Sunburst Arc. In the remainder of this section, we first highlight the peculiar nature of slit M3, which contains a peculiar source and a triple-peaked Ly α profile, but no significant escaping LyC flux. We then discuss possible explanations for all of the observed Ly α profiles in the MagE spectra.

5.1. A Triple-peaked Ly α Profile without LyC Escape

Slit M3 stands out as the only non-LyC-leaking aperture with a triple-peaked Ly α profile, including a blueshifted Ly α peak with a slightly smaller blueshifted velocity than the blueshifted Ly α peak in the LyC-leaking apertures. The brightest continuum source in slit M3 (image 4.8 in Figure 1) has been dubbed T_r (E. Vanzella et al. 2020b), Godzilla (J. M. Diego et al. 2022; S. Choe et al. 2024; M. Pascale & L. Dai 2024), and “the discrepant clump” (K. Sharon et al. 2022). The literature favors this object as stellar in nature, and we will refer to it as image 4.8, following K. Sharon et al. (2022). Here we discuss the Ly α and LyC escape properties of this object.

A natural starting assumption is to attribute the Ly α emission in slit M3 to the brightest continuum source captured by the slit, which is image 4.8. However, the Ly α narrowband maps from the WFC3/F410M image reveal that image 4.8 itself is mostly likely a net Ly α absorber, with the other diffuse arc flux that falls into slit M3 producing the observed Ly α emission. Inspecting slit M3’s position in the source-plane reconstruction indicates that the emission captured by slit M3 comes from two physically distinct parts of the galaxy: region 4, and diffuse emission from or between regions 1, 2, and 5. This is notable because this diffuse emission in slit M3 comes from a region that is closer to the LyC-leaking region (but without containing the LyC-leaking region itself) than any other of the MagE slit apertures.

We observe LyC flux in slit M3’s aperture statistically consistent with zero flux (at 2σ confidence; Table 3). However, the young age (~ 4 Myr), low stellar extinction of $E(B - V) = 0.018$ (the lowest measured in the MagE data; R. Mainali et al. 2022), and narrow Ly α peak separation

suggest a low H I column density and a favorable stellar population and line of sight for LyC escape. However, it is difficult to tie all of these characteristics to the same physical region, since slit M3 covers emission regions separated by ~ 1 kpc in the source plane (Figure 7). Here we review how the different physical natures offered for image 4.8 in the literature connect to the Ly α and LyC observations presented in this paper.

1. *A supernova.* E. Vanzella et al. (2020b) first discussed the main image’s identity, positing it to be a transient stellar object, evidenced by the lack of counterimages and the lack of any other object with the same unique spectroscopic signatures, namely Bowen fluorescence (I. S. Bowen 1934). Based on their predicted magnification ($20 < \mu < 100$) and corresponding absolute magnitude ($-20.3 < M_{2000} < -18.6$) of the main image, they favored a supernova and disfavored a LBV star as too faint. However, detailed lens modeling by J. M. Diego et al. (2022) and K. Sharon et al. (2022) jointly corroborated that (1) the magnification of the main image must be extremely high ($\mu > 600$), (2) the source-plane persistence of the main image is exceptionally long for a supernova (> 1 yr), and (3) the predicted time delays for this source between different images (< 1 yr) are significantly shorter than the elapsed time of observations. The lack of appearance of any new, comparably bright images of “Godzilla” over > 7 yr strongly disfavors the supernova hypothesis. The lack of Ly α and LyC emission from image 4.8 is consistent with a SN.
2. *A LBV star.* In contrast, J. M. Diego et al. (2022) suggested the largest knot in slit M3 could be a LBV star in outburst. This could explain the observed Ly α signature and faint LyC detection, as well as rest-UV spectral features (E. Vanzella et al. 2020b). Quiescent LBVs are often B-type stars with temperatures ranging between $\sim 10,000$ and $25,000$ K, but during their outbursts they cool to ~ 8500 K and shed their outer layers as large mass outflows. Assuming the star’s quiescent temperature is among the hotter LBVs, the star may produce appreciable LyC flux. The radiative and mechanical energy from the LBV during an active phase could clear an underdense channel in the surrounding H I, but this picture is in tension with S. Choe et al. (2024), who concluded from JWST/NIRSpec integral field unit (IFU) observations that the main image is a quiescent LBV, not an outbursting LBV. Furthermore, the dense gas required to pump Bowen fluorescence would naturally suppress escaping Ly α and LyC emission from the LBV, consistent with the observed lack of Ly α and LyC emission from image 4.8.

As we explore physical hypotheses to explain the observed Ly α profiles below, it is important to remember that any plausible scenario must explain how slit M3 could show both central and blueshifted Ly α peaks but no escaping LyC photons.

5.2. Seeing Effects

We have considered if ground-based seeing conditions cause the unique kinematic structure of the Ly α profiles of the non-LyC-leaking apertures by diffusing images of the LyC leaker’s triple-peaked Ly α profile into non-LyC-leaking apertures. To

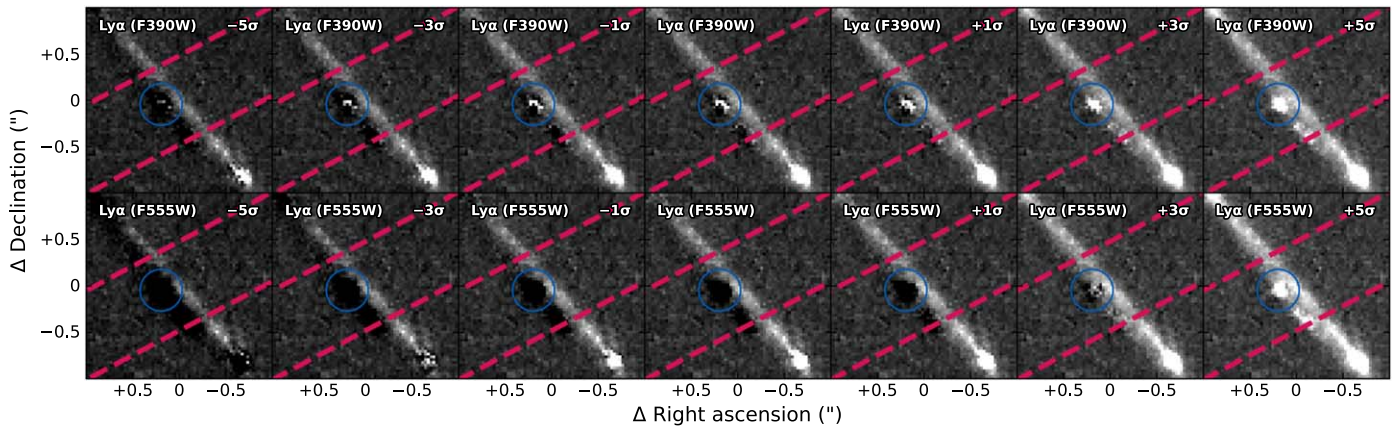


Figure 8. Ly α maps centered on slit M3 created from the schemes discussed in Section 3.3. The top and bottom rows show the maps with the F390W and F555W filters as the off-band filter, respectively. The dashed magenta line is the on-sky aperture of slit M3. There are systematic differences between the two continuum subtraction bands, with the F555W-based subtraction removing marginally more continuum flux than the F390W-based subtraction.

Table 6
Simulated Aperture Flux Changes Due to Atmospheric Seeing

Slit	Unconvolved ($e^- s^{-1}$)	F390W Convolved ($e^- s^{-1}$)	Ratio	Unconvolved ($e^- s^{-1}$)	F555W Convolved ($e^- s^{-1}$)	Ratio
M5	0.82 ± 0.03	0.86 ± 0.03	1.05 ± 0.05	-0.15 ± 0.04	-0.21 ± 0.04	1.4 ± 0.5
M4	1.34 ± 0.03	1.42 ± 0.03	1.06 ± 0.03	0.04 ± 0.04	0.35 ± 0.04	10 ± 10
M6	1.66 ± 0.03	1.80 ± 0.03	1.08 ± 0.02	0.49 ± 0.04	0.81 ± 0.04	1.6 ± 0.2
M3	1.51 ± 0.04	1.61 ± 0.04	1.06 ± 0.04	-0.24 ± 0.08	0.25 ± 0.08	-1.0 ± 0.5
M0	5.90 ± 0.06	4.40 ± 0.06	0.75 ± 0.01	3.6 ± 0.1	2.8 ± 0.1	0.78 ± 0.04
M2	6.63 ± 0.07	5.10 ± 0.07	0.77 ± 0.01	5.2 ± 0.1	4.0 ± 0.1	0.77 ± 0.03
M7	3.22 ± 0.04	2.50 ± 0.04	0.78 ± 0.01	2.18 ± 0.07	1.70 ± 0.07	0.78 ± 0.04
M8	2.49 ± 0.02	2.21 ± 0.02	0.89 ± 0.01	1.98 ± 0.04	1.79 ± 0.04	0.90 ± 0.03
M9	3.02 ± 0.03	2.43 ± 0.03	0.80 ± 0.01	2.27 ± 0.06	1.46 ± 0.06	0.64 ± 0.03

Note. From left to right: slit; flux inside the slit of the unconvolved and simulated seeing-convolved F390W-based Ly α map; the ratio between the two fluxes; and likewise for the F555W-based Ly α map. Ratios >1 indicate the flux in the aperture increased after the convolution, and ratios <1 indicate the flux in the aperture decreased after the convolution. The convolution used a two-dimensional Gaussian kernel of the combined effect of the time-weighted seeing conditions and air masses (Section 5.2).

judge this, we simulated the atmospheric diffusion with the Ly α maps discussed in Section 3.3. For each slit aperture, we convolved each Ly α map with a two-dimensional Gaussian kernel with width matching the time-weighted average of the combined effect of the seeing conditions (see Table 1 for a time-weighted average of the seeing conditions for each slit) and air mass for each exposure (Table 1). We then calculated the flux inside each slit aperture before and after the convolution and the ratio between those fluxes for each Ly α map. Table 6 contains the results.

In both the Ly α maps made from the F555W- and F390W-based continuum subtraction, we found that the LyC-leaking apertures lose Ly α flux ($\sim 10\%$ – 40%) and the non-LyC-leaking slits mostly gain Ly α flux ($\sim 5\%$ – 800%). The one exception is slit M5, which has a pre- and post-convolution flux that is statistically consistent to within $\sim 2\sigma$ in both continuum subtraction schemes.

We now outline how each non-LyC-leaking aperture fits into the seeing-effects hypothesis, roughly in order of the apertures nearest to farthest from images of the LyC-leaking region on the sky:

1. Slit M3 is roughly the non-LyC-leaking aperture nearest to images of the LyC-leaking region (Figure 4) and the

only non-LyC-leaking aperture that has a blueshifted Ly α peak. This slit is the most consistent with the seeing-effects hypothesis since it shows the hallmark triple-peaked Ly α profile of the LyC leaker and is $<1''$ away from the nearest image of the LyC-leaking region. Slit M3's Ly α flux either changes significantly or minimally in the simulated seeing convolution, depending on the Ly α map (Table 6). This ambiguity is because the F555W-based Ly α map predicts strong Ly α absorption near and on the images in slit M3 (Figure 8). Additionally, slit M3's blueshifted Ly α peak is distinctly closer to the systemic redshift than the blueshifted Ly α peaks observed from the LyC-leaking region (Figure 2, Table 7), which point to a different physical origin for slit M3's blueshifted Ly α peak than simple seeing effects.

2. Slit M4 is farther from the nearest images of the LyC-leaking region than slit M3, but still close enough ($\sim 1''$) that seeing effects could cause some contamination (Figure 4). Similar to slit M3, the Ly α flux in the aperture either changes significantly or minimally after the simulated seeing convolution, depending on the Ly α map (Table 6). Most importantly, slit M4 does not show a blueshifted Ly α peak (Figure 2), which we would expect

Table 7
Ly α Modeling Best-fit Parameters

Slit	Blue Peak	Red Peak	Central Peak	Continuum
NL	-/-/-/-	$3.74^{+0.07}_{-0.07}/127^{+5}_{-5}/210^{+4}_{-4}/3.5^{+0.4}_{-0.3}$	$2.3^{+0.3}_{-0.3}/60^{+5}_{-5}/41^{+2}_{-3}/-$	$1.17^{+0.02}_{-0.02}$
L	$6.58^{+0.07}_{-0.07}/-99^{+2}_{-2}/89^{+2}_{-2}/-0.0002^{+0.0002}_{-0.0003}$	$5.7^{+0.1}_{-0.1}/157^{+5}_{-5}/210^{+3}_{-2}/5.3^{+0.9}_{-0.8}$	$22.6^{+0.3}_{-0.4}/79^{+1}_{-1}/41^{+1}_{-1}/-$	$1.34^{+0.02}_{-0.02}$
M5	-/-/-/-	$1.91^{+0.06}_{-0.06}/121^{+5}_{-4}/204^{+7}_{-7}/5.1^{+1}_{-0.7}$	$0.6^{+0.3}_{-0.2}/40^{+20}_{-10}/30^{+10}_{-10}/-$	$0.92^{+0.02}_{-0.02}$
M4	-/-/-/-	$1.93^{+0.07}_{-0.07}/128^{+4}_{-4}/194^{+6}_{-6}/6^{+1}_{-1}$	$1.7^{+0.1}_{-0.1}/44^{+6}_{-5}/36^{+5}_{-4}/-$	$0.69^{+0.02}_{-0.02}$
M6	-/-/-/-	$3.15^{+0.1}_{-0.07}/175^{+3}_{-3}/193^{+4}_{-4}/6^{+1}_{-2}$	$5.1^{+0.2}_{-0.2}/95^{+3}_{-6}/45^{+2}_{-3}/-$	$0.87^{+0.02}_{-0.02}$
M3	$3.56^{+0.08}_{-0.09}/-66^{+6}_{-6}/81^{+4}_{-4}/-0.0004^{+0.0004}_{-0.0004}$	$2.96^{+0.07}_{-0.07}/168^{+3}_{-4}/184^{+4}_{-3}/5.0^{+0.9}_{-0.8}$	$7.5^{+0.2}_{-0.3}/77^{+2}_{-2}/42^{+2}_{-2}/-$	$0.65^{+0.01}_{-0.01}$
M0	$55.4^{+0.9}_{-0.9}/-105^{+2}_{-2}/79^{+2}_{-2}/-0.0009^{+0.0008}_{-0.0002}$	$48.5^{+0.8}_{-0.7}/186^{+2}_{-3}/202^{+3}_{-3}/6.5^{+0.7}_{-0.7}$	$208^{+2}_{-2}/94.5^{+0.7}_{-0.8}/46.6^{+0.9}_{-1}/-$	$13.3^{+0.2}_{-0.2}$
M2	$3.6^{+0.2}_{-1}/-102^{+70}_{-7}/85^{+40}_{-5}/-0.05^{+0.05}_{-3}$	$3.8^{+0.2}_{-0.2}/160^{+10}_{-10}/197^{+6}_{-5}/4^{+2}_{-1}$	$18.1^{+0.5}_{-0.8}/84^{+2}_{-1}/38^{+3}_{-1}/-$	$0.99^{+0.03}_{-0.03}$
M7	$5.22^{+0.07}_{-0.07}/-103^{+3}_{-3}/89^{+2}_{-2}/-0.0008^{+0.0008}_{-0.0003}$	$4.01^{+0.06}_{-0.05}/150^{+2}_{-3}/203^{+2}_{-3}/7.4^{+0.8}_{-0.9}$	$16.1^{+0.2}_{-0.2}/67.7^{+0.7}_{-0.8}/40.6^{+0.9}_{-1}/-$	$0.94^{+0.01}_{-0.01}$
M8	$4.77^{+0.07}_{-0.07}/-91^{+3}_{-3}/87^{+3}_{-3}/-0.0006^{+0.0006}_{-0.0003}$	$4.08^{+0.1}_{-0.07}/168^{+3}_{-7}/212^{+4}_{-3}/7^{+1}_{-2}$	$16.6^{+0.2}_{-0.3}/86^{+1}_{-2}/42^{+1}_{-2}/-$	$0.89^{+0.02}_{-0.02}$
M9	$2.89^{+0.08}_{-0.08}/-100^{+5}_{-4}/88^{+5}_{-4}/-0.001^{+0.001}_{-0.004}$	$2.42^{+0.06}_{-0.05}/170^{+2}_{-3}/213^{+5}_{-5}/8^{+2}_{-2}$	$9.6^{+0.2}_{-0.2}/80^{+1}_{-1}/43^{+1}_{-1}/-$	$0.66^{+0.02}_{-0.02}$

Notes. Best-fit Ly α parameters of the magnification-uncorrected, rest-frame Ly α profiles. From left to right: slit label; best-fit parameters for the blueshifted peak, redshifted peak, and central peak, presented as $\alpha/\mu/\sigma/\omega$, as described in Section 3.5.4, and the local continuum flux density. Apart from the stacked spectra, α and the local continuum flux density have units of 10^{-16} erg s $^{-1}$ cm $^{-2}$ Å $^{-1}$, μ and σ have units of kilometers per second.

^a The fitted amplitudes of slit M0 are significantly different from the other observations because this observation was taken through cloud cover that prevented an accurate fluxing. See Table 1 for more information about the observing conditions.

to see if significant Ly α flux from the LyC-leaking region diffused into this slit due to seeing effects.

- Slit M6 is well separated from the closest images of the LyC-leaking region (Figure 4), but still has a strong central Ly α peak, though no blueshifted Ly α peak. At most, the seeing-convolved Ly α images predict a moderately increased Ly α flux due to seeing effects. The absolute, magnification-uncorrected strength of slit M6’s central Ly α peak is several times greater than that of slit M4 (Table 7), even though slit M4 is closer to images of the LyC-leaking region. This fact (and the nonobservation of a blueshifted Ly α peak) strongly disfavors the seeing-effects hypothesis since an aperture (slit M6) farther from images known to emit a central Ly α peak has a stronger central Ly α peak than another, closer aperture (slit M4).
- Slit M5 shows no distinct central or blueshifted Ly α peak and is one of the non-LyC-leaking apertures farthest from images of the LyC leaker (Figure 4), which is consistent with the seeing-effects hypothesis. Like slit M6, the simulated seeing convolution predicts a minimal or moderate increase in Ly α flux in the slit M5 aperture due to the observing conditions (Table 6).

Combined, the evidence above suggests seeing effects alone cannot explain all the Ly α profiles of the non-LyC-leaking apertures, but might affect their Ly α profiles in some instances, such as slit M3 due to its proximity to images of the LyC-leaking region. Because both ground-based seeing effects (Section 5.2) and differential magnification from gravitational lensing do not explain the observed Ly α profiles of the non-LyC-leaking apertures, we must consider explanations that invoke complex mechanisms and morphologies, which we explore below.

5.3. Multiple Direct-escape Ly α Channels

Here we consider if additional ionized channels might also explain the central Ly α peaks observed from the non-LyC-leaking apertures. Any channel-escape scenario must explain the observation of a central Ly α peak but not a blueshifted Ly α

peak in some of the non-LyC-leaking apertures (slits M4 and M6). If the additional ionized channels are similar to the channel observed in the LyC-leaking region (i.e., additional small channels puncturing an isotropically expanding H I shell), then the gas along the sight lines toward the additional channels must have properties that permit Ly α photons to directly escape, but not LyC photons.

Such a scenario is difficult to construct because the cross section for Ly α photons to interact with H I is $\sim 10^4$ times higher than the cross section for LyC photon interactions. This means that if there is sufficiently low H I column density along a sight line to allow Ly α photons to escape with few or no scattering events (“direct-escape” Ly α), then LyC photons should also freely escape. Furthermore, a blueshifted Ly α peak is associated with outflowing gas with low H I column density. The lack of a blueshifted Ly α peak in some of the non-LyC-leaking apertures with a central Ly α peak requires either (1) simultaneously both high column density, outflowing H I and an extremely low column density H I channel puncturing it, or (2) a complete absence of outflowing H I. The former would require a sharp transition between the two gas phases to minimize the H I thin enough to transmit a blueshifted Ly α peak but thick enough to prevent direct Ly α escape, while the latter would allow LyC photons to efficiently escape (which we do not observe).

We also note that the stellar populations in the non-LyC-leaking regions of the Sunburst Arc have ages of 11.8 ± 0.9 Myr (R. Mainali et al. 2022), which is notably older and should produce fewer LyC photons (X. Ma et al. 2015, 2020; T. Kimm et al. 2017; J.-G. Kim et al. 2019; K. Kakiichi & M. Gronke 2021) than the LyC-leaking region’s age of 3.3 ± 0.5 Myr (R. Mainali et al. 2022). The rest-UV absorption lines and nebular emission lines in the non-LyC-leaking spectra also indicate weaker stellar winds, bulk outflows (R. Mainali et al. 2022), and less extreme ionizing radiation fields (K. J. Kim et al. 2023) than the LyC-leaking region, meaning the non-LyC-leaking regions are less well suited to create ionized channels. This makes it physically unlikely for the non-LyC-leaking regions to be able to create additional highly ionized channels, especially considering that

radiative transfer simulations predict channels to be extremely rare (e.g., C. Behrens et al. 2014).

5.4. A Ly α Mirror

We now introduce a Ly α “mirror” hypothesis, which posits that dense H I cores could preferentially scatter Ly α photons from the LyC-leaking region into our sight line far from their origin. As discussed in Section 1, Ly α photons may wander far from their birthplace before scattering into our sight line. The central Ly α peak observed in some of the non-LyC-leaking apertures might be an extreme case of this: Ly α photons of the LyC-leaking region incident upon dense H I gas surrounding the non-LyC-leaking regions may preferentially scatter off of the cores’ surfaces and cause apparent Ly α emission from regions physically distant from the original Ly α source.

This preferential scattering is similar to the mechanism that produces the redshifted Ly α peak in an isotropically expanding H I shell geometry (e.g., Figure 12 in A. Verhamme et al. 2006). If this process involved only a few scatterings then the central Ly α peak may survive, albeit diminished, which is what we observe in the non-LyC-leaking apertures that are closest to the LyC-leaking region in the source plane (Figure 2). This would require either a large region with very low column density H I and/or very fast (i.e., out of resonance) outflowing gas between the “mirror” and our sight line to allow the central Ly α photons to escape. The strong ionizing photon flux of the LyC-leaking region may aid this process by creating a large ionized region inside the galaxy, allowing Ly α photons to traverse large distances far from their birthplace. Figure 9 sketches out this hypothesis.

We now outline how this hypothesis connects to the Ly α profiles of each non-LyC-leaking aperture, in order of the strongest to weakest central Ly α peaks, relative to their associated redshifted Ly α peaks.

1. Slit M3 covers parts of regions 1, 2, 4, 5, and 9 in the source plane (Figure 7). Slit M3 is the closest non-LyC-leaking aperture to the LyC-leaking region, meaning some of the area it covers—namely regions 1, 2, and 5—could receive the necessary Ly α flux to scatter into our sight line before significant Ly α photons scatter prematurely, attenuate, or become too diffuse. If a Ly α “mirror” causes slit M3’s strong central Ly α peak, there must be very few scatterings and a strong directional bias toward us to preserve a central Ly α peak that is nearly as strong (relative to the spectrum’s other Ly α peaks) as in the LyC-leaking apertures. There must also be very low column density outflowing H I in this region to explain the presence of a blueshifted Ly α peak in slit M3. The lack of LyC photons within this aperture suggests that there are no bright LyC photon sources in the diffuse emission captured by slit M3, such that the Ly α emission detected from this slit is the product of Ly α photons that diffused away from the LyC-leaking region before scattering into our sight line.
2. Slit M6 covers parts of regions 2, 5, and 8. Slit M6’s central Ly α peak is comparable in strength to its redshifted Ly α peak (Figure 2), and its projected distance to the LyC-leaking region in the source plane is farther than for slit M3 (Figure 7). The central Ly α peak of slit M6 could also result from the “mirror” effect. Slit M6’s larger distance from the LyC-leaking region might

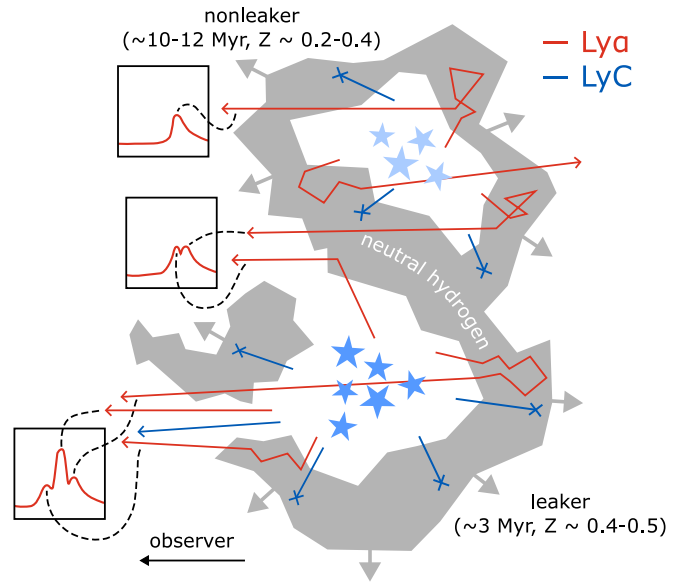


Figure 9. Cartoon of the Ly α mirror hypothesis. The LyC-leaking region (bottom) produces a prodigious amount of Ly α (red) and LyC (blue) photons compared to the older non-LyC-leaking regions (top). Some photons from the LyC-leaking region directly escape out of a highly ionized channel oriented toward us. These photons constitute the observed LyC and central Ly α peak. Additional Ly α emission resonantly scatters off the expanding H I surrounding the LyC-leaking region until it escapes the galaxy along the observer’s sight line, which constitute the redshifted and blueshifted Ly α peaks (bottom box). In the non-LyC-leaking regions, which have much less LyC flux due to their older age, the surrounding H I (gray) is thicker, preventing any LyC escape and direct Ly α escape. Thus, only a redshifted Ly α peak emerges (first box from the top). However, Ly α photons from the LyC-leaking region preferentially reflect into the observer’s sight line incident upon the thick H I around the non-LyC-leaking regions (second box from the top), forming a central Ly α peak superimposed upon the redshifted Ly α peak emerging from the non-LyC-leaking regions.

explain the weaker central Ly α peak (relative to the redshifted Ly α peak) compared to the LyC-leaking region due to some combination of (1) a smaller covering fraction of the mirror for slit M6 than slit M3, and (2) an increasing number of scattering events for Ly α photons as they travel farther from their original source in the LyC-leaking region.

3. Slit M4 targets a lower-magnification region of the arc and therefore covers a large portion of the lensed galaxy in the source plane, including regions 2–11. Though parts of the slit are closer to the LyC-leaking region in the source plane than slit M6 (Figure 7), its central Ly α peak is much weaker compared to its redshifted Ly α peak than in slit M6, though the magnification-corrected central Ly α flux is still stronger absolutely than that of slit M6 (Figure 2, Table 7). This makes sense given the large footprint of slit M4 in the source plane if the redshifted Ly α peak is a global feature while the central Ly α peak is not.
4. Slit M5 covers parts of regions 3, 8–10, and 13–15. Of all the non-LyC-leaking apertures, it has the largest projected distance from the LyC-leaking region in the source plane, and it is the only non-LyC-leaking aperture with no clear central Ly α peak. This implies a minimum upper limit on the extent of the central Ly α peak of $\lesssim 800$ pc.

If a Ly α mirror does exist, it extends to at least clumps 1, 2, 5, and 9 in Figure 7, since those clumps define a region of

overlap between slits that show a central Ly α peak (M3, M4, and M6). This suggests a direct-escape Ly α region extending as much as $\sim 600\text{--}800$ pc from the LyC-leaking region.

5.5. Spatially Variable Ly α Absorption

The final hypothesis we present also relies on a complex H I morphology in the source plane. We suggest that the triple-peaked Ly α profile of the LyC-leaking region occupies an area in the source plane that is much larger than the clump producing the ionizing radiation (the LyC-leaking region). In this picture, the LyC-leaking region has ionized a huge volume of gas, producing the central Ly α peak over a large extent, as escaping Ly α photons can either form in situ from the extended ionized gas, or travel large transverse distances in the source plane before experiencing scattering event(s) that redirect them into other, non-LyC-leaking sight lines.

The spatial variability of the blueshifted and central Ly α peaks' strength is likely due to an outflowing (blueshifted) intervening absorber with H I column density that varies spatially across the face of the galaxy. For this absorber to screen the central Ly α peak, there must be additional highly ionized sight lines toward the extended ionized gas. For example, the H I surrounding the extended ionized gas may be patchy and heavily punctured. However, the H I cannot be significantly perforated, or there would not be sufficient approaching, outflowing H I to reprocess Ly α photons into the blueshifted Ly α peak that we see in slit M3 and the LyC-leaking apertures. Figure 10 depicts the basic principles of this scenario.

There are several key unknowns involved in this picture. First, what is the size and structure of the highly ionized, extended region around the LyC-leaking region? Second, what is the location and morphology of the neutral H I gas that absorbs LyC photons from all sight lines except those from a small channel toward the LyC-leaking region? The first question could be addressed in part by future spatially resolved measurements of the physical extent of forbidden (optically thin) nebular emission lines in the source plane. The second question, however, may require very specific H I morphology and kinematics to efficiently diffuse the directly escaping, central Ly α peak from the LyC-leaking region without completely rescattering it—perhaps not too dissimilar from the H I morphology and kinematics presumed in the mirror hypothesis of Section 5.4—if most of the central Ly α peak's photons do not form in situ from the extended ionized gas.

Significant supporting evidence exists for this hypothesis. For instance, the neutral-gas-tracing low-ionization absorption analyzed by R. Mainali et al. (2022) suggests a blueshifted, low-ionization absorber exists along both LyC-leaking and non-LyC-leaking sight lines. That result is also consistent with the absorption trough at ~ -350 km s $^{-1}$ (Figure 2) that is present in *all* of the Ly α spectra. Furthermore, this blueshifted absorption trough has noticeably stronger absorption tails in the non-LyC-leaking MagE spectra, suggesting an absorption gradient between the LyC-leaking and non-LyC-leaking regions, with an increasing column density as the slits move farther away from the LyC-leaking region. This absorber might also explain the sharp drop-off on the blue side of the blueshifted Ly α peaks. Below, we explore how each non-LyC-leaking aperture might fit into this picture, in order of increasing projected distance from the LyC-leaking region,

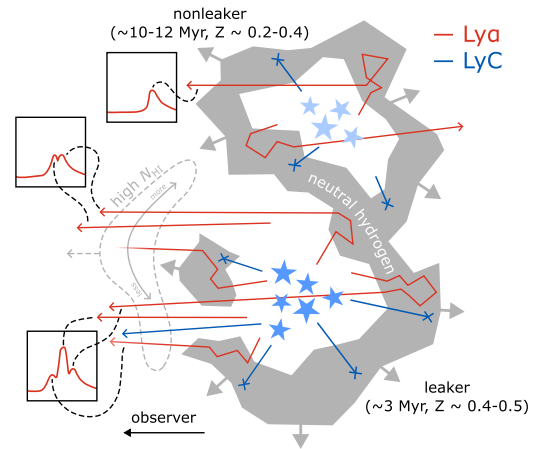


Figure 10. Cartoon sketch of the spatially variable absorption hypothesis. The Ly α and LyC photons directly escaping through an ionized channel produce the LyC and the central Ly α peak observed from the LyC-leaking region. Ly α photons from the LyC-leaking region also resonantly scatter with either side of the surrounding, expanding H I shell, forming the redshifted and blueshifted Ly α peaks (bottom box). In this picture, the triple-peaked Ly α profile from the LyC-leaking region originates from a large source-plane area, and an intervening, outflowing absorber with higher H I column density attenuates the blueshifted Ly α peak and varying amounts of the central Ly α peak across the face of the galaxy.

based on the source-plane reconstruction (Figure 7) and Ly α profile fits (Figure 2).

1. Of the non-LyC-leaking apertures, slit M3 is nearest to the LyC-leaking region in the source plane. It also shows the least signs of absorption compared to the LyC-leaking region's Ly α profile, all of which is fully consistent with this physical picture. A very weak absorption process also provides the simplest and clearest explanation for slit M3's blueshifted Ly α peak, which is slightly less blueshifted than the blueshifted Ly α peak in the LyC-leaking spectra. Similar to the Ly α mirror hypothesis above, the lack of LyC photons within this aperture suggests that all of the Ly α photons observed in slit M3 stem from Ly α photons that diffused or originated far from the LyC-leaking region before entering our sight line.
2. Slit M4 is the next-closest slit to the LyC-leaking region in the source plane, though it also has the largest footprint and captures many non-LyC-leaking regions distant from the LyC-leaking region. Slit M4 shows a suppressed central Ly α peak and no blueshifted Ly α peak. In the gradient absorber picture, this would indicate the absorber's optical depth has grown, which is consistent with the increased distance of slit M4 to the LyC-leaking region in the source plane.
3. Slit M6 has a very high magnification ($\mu = 147^{+5}_{-20}$, Table 1), causing the slit to be very narrow in the source plane, isolating region 2. Slit M6 is an interesting contrast to slit M4 (which is one of the least magnified slits). Comparing the total, magnification-corrected flux in the central Ly α peaks of slits M6 and M4, there is significantly more flux in slit M4, but comparing the *relative* strengths of the central and redshifted Ly α peaks, it is clear slit M6's central Ly α peak is stronger relative to the redshifted Ly α peak than in slit M4. This makes sense if (1) the redshifted Ly α peak is a global emission feature

with approximately constant surface brightness across the entire source plane, and (2) the central Ly α peak emission is localized to a region that extends a few hundred parsecs around the LyC-leaking region. Slit M4 has a much larger footprint that could then contain Ly α profiles from other non-LyC-leaking regions (which slit M6 does not cover) with higher HI column densities and a more diminished or absent central Ly α peak and stronger absorption trough.

4. Slit M5 is the farthest aperture from the LyC-leaking region in the source plane. It has no clear evidence of any residual blueshifted or central Ly α peak. Its Ly α profile could be consistent with a single redshifted Ly α peak. This slit is consistent with the redshifted Ly α peak as a global emission feature that extends across the entire galaxy. If the central Ly α peak’s production region extends as far as slit M5 in the source plane, then the intervening absorber along this slit’s sight line must have a very high HI column density to suppress the central Ly α emission. It is also possible that the physical extent of the region emitting the central Ly α peak ends somewhere between slits M6 and M5 in the source plane.

Combined, we believe that a diffuse triple-peaked Ly α profile combined with blueshifted HI absorption as a physical scenario has significant merit, especially considering the ubiquitous absorption trough in every Ly α profile.

6. Conclusions

In this work, we analyzed rest-UV, high-resolution ($R \sim 5000$) spectroscopy of the Ly α emission line in the Sunburst Arc (Section 2.1), a strongly lensed, LyC-leaking galaxy at $z \approx 2.37$. We directly fitted the Ly α velocity profiles to extract key parameters (Section 3.5) such as the peak separation v_{sep} (Section 3.5.4), peak widths (Section 3.5.4), Ly α EW (Section 3.5.2), central escape fraction f_{cen} (Section 3.5.3), and ratio between the minimum flux density between the peaks and local continuum flux density $f_{\text{min}}/f_{\text{cont}}$ (Section 3.5.5). Using HST imaging (Section 2.2), we computed the LyC escape fractions associated with the spectroscopic observations (Section 3.4).

From this, we computed statistical correlations between the Ly α and LyC parameters to better understand their interdependence (Section 4), and offered brief discussion of the measurements of each parameter (Sections 4.1, 4.2.1–4.2.5) and possible shortcomings of the Ly α profile fitting (Section 4.2). In short, we found the following:

- (i) A strong positive correlation between $f_{\text{esc}}^{\text{LyC}}$ and v_{sep} , $f_{\text{min}}/f_{\text{cont}}$, and Ly α EW (Table 5).
- (ii) Few clear relations between any two parameters involving any of the Ly α peak widths (Table 5).
- (iii) Affirmations of previously suggested relations, especially a strong correlation between the Ly α EW and $f_{\text{min}}/f_{\text{cont}}$.

We also note that a central Ly α peak appears even in spectra of non-LyC-leaking regions from apertures located within ~ 600 pc of the LyC-leaking region. We briefly discussed the observed spectrum of the highly magnified region known as “Godzilla” and its implications for the nature of the object. Based upon the data and a source-plane reconstruction of the slit aperture geometry (Figure 7), we discussed several possible

explanations for the diversity of Ly α profiles observed in the Sunburst Arc (Section 5), particularly those from the non-LyC-leaking spectra. We first considered if ground-based seeing effects (Section 5.2) could cause the observed Ly α profiles by diffusing emission from images of the LyC-leaking region into the non-LyC-leaking slit apertures, but concluded that this mechanism cannot explain the data.

We then discussed physical mechanisms to explain the observed Ly α profiles of the non-LyC-leaking apertures (Sections 5.3–5.5). We concluded that the data are inconsistent with the presence of additional highly ionized channels that permit direct Ly α escape without LyC escape (Section 5.3). We then sketched out two physical scenarios, the Ly α mirror (Section 5.4) and the spatially variable Ly α absorber (Section 5.5), to explain the presence of a central Ly α peak that originates from a much larger physical region than the escaping LyC photons.

The hypotheses we judged to be the strongest both invoke some form of spatially variable HI with complex morphology, geometry, and/or kinematics which can efficiently diffuse and/or preferentially rescatter a central Ly α peak, likely from the LyC-leaking region. In one scenario (Section 5.4), dense but perforated HI in the intermediate space between the LyC-leaking and non-LyC-leaking regions preferentially rescatters a central Ly α peak into our sight line with minimal velocity shift. In the second scenario (Section 5.5), the central Ly α peak actually occupies a much larger area in the source plane than the LyC-leaking region. Although the specific HI structure and role of absorption are unclear in this explanation, additionally invoking a blueshifted absorber likely offers the simplest explanation and is also consistent with the ubiquitous blueshifted Ly α absorption feature centered around -350 km s^{-1} . Low-ionization metal absorption lines seen toward the non-LyC-leaking regions also support the existence of such an absorber (R. Mainali et al. 2022).

Another important implication of the work presented here is the direct measurement of the complex, anisotropic relationship between the escape of Ly α and LyC photons, particularly on the small physical scales (hundreds of parsecs and less) probed in the strongly lensed Sunburst Arc. The individual ISM structures that shape Ly α and LyC escape vary at or below this physical scale, which may challenge intuition built from galaxy-integrated properties. The Sunburst Arc is an instructive example of this variability and the small, complex ISM structures we must consider as we develop our understanding of the Ly α –LyC connection at subgalactic scales. The central Ly α peaks without corresponding LyC escape presented in this work are a clear example of this conflict.

As wide-area surveys such as DECaLS, Pan-STARRS, the Sloan Digital Sky Survey, and soon Rubin’s Legacy Survey of Space and Time or the Roman Space Telescope’s High Latitude Wide Area Survey discover increasing numbers of strongly lensed galaxies, JWST and ELTs will target them with extremely sharp imaging and IFU spectroscopy. We will be able to routinely map distant galaxies down to scales of tens of parsecs or less. Until the discovery of more exceptional objects, the Sunburst Arc offers the highest-spatial-resolution view of the Ly α and LyC escape processes, and the best opportunity to reconcile disagreements between low- and high-spatial-resolution Ly α and LyC observations.

Acknowledgments

M.R.O. would like to thank the authors of N. Chamba et al. (2022) and J. H. Knapen et al. (2022) for the helpfulness of their works during the initial development of this manuscript. This paper is based on data gathered with the 6.5 m Magellan Telescopes located at Las Campanas Observatory, Chile. This work is also based, in part, on observations made with the NASA/ESA Hubble Space Telescope obtained from the Space Telescope Science Institute, which is operated by the Association of Universities for Research in Astronomy, Inc., under NASA contract NAS 5-26555. These observations are associated with programs GO-15101 (PI: H. Dahle), GO-15377 (PI: M. Bayliss), GO-15418 (PI: H. Dahle), and GO-15949 (PI: M. Gladders). This work was supported by grants associated with programs GO-15101, GO-15377, GO-15418, and GO-15949 that were awarded by STScI under NASA contract NAS 5-26555. T.E.R.-T. is supported by the Swedish Research Council grant No. 2022-04805_VR. Data presented in this paper were obtained from the Mikulski Archive for Space Telescopes (MAST) at the Space Telescope Science Institute. The specific observations analyzed can be accessed via doi:10.17909/t87g-a816. STScI is operated by the Association of Universities for Research in Astronomy, Inc., under NASA contract NAS 5-26555. Support to MAST for these data is provided by the NASA Office of Space Science via grant NAG5-7584 and by other grants and contracts. Support for this work was provided by the National Aeronautics and Space Administration through Chandra Award Number GO1-22081X issued by the Chandra X-ray Center, operated by the Smithsonian Astrophysical Observatory for and on behalf of the National Aeronautics Space Administration under contract NAS8-03060. This work also makes use of the SAO/NASA Astrophysics Data System’s bibliographic services. We prepared this manuscript using the colorblindness simulation tool created by David Nichols (<https://davidmathlogic.com/colorblind/>) to create figures accommodating colorblindness.

Facilities: HST (ACS, WFC3), Magellan:Baade (FIRE, MagE).

Software: asciitree, Astropy (Astropy Collaboration et al. 2013, 2018, 2022), astropy-iers-data (T. Robitaille et al. 2024), astropy-healpix, asttokens, Beautiful Soup, Click, cloudpickle, Colorama, Comm, ContourPy, cycler, Dask (<https://docs.dask.org/en/stable/>), debugpy, decorator, executing, extinction, Fasteners, fonttools, fspec, GALFIT (C. Y. Peng et al. 2010), ipykernel, IPython (F. Perez & B. E. Granger 2007), Jedi, Jupyter Client, Jupyter Core, Jupyter Notebooks (T. Kluyver et al. 2016), kiwisolver, lazy_loader, llvmlite, Locket, Matplotlib (J. D. Hunter 2007; The Matplotlib Development Team 2024), matplotlib-inline, nest-asyncio, Numba (S. K. Lam et al. 2015), Numcodecs, NumPy (C. R. Harris et al. 2020), packaging, pandas (W. McKinney 2020; The pandas development team 2024), Parso, PartD, Photutils (L. Bradley et al. 2024b), Pillow (A. Murray et al. 2024), platformdirs, prompt_toolkit, prospector (B. D. Johnson et al. 2021), psutil, pure_eval, PyERFA, Pygments, pyparsing, python-dateutil, pytz, pywin32, PyYAML, PyZMQ, Regions (L. Bradley et al. 2024a), reproject, scikit-image (S. J. van der Walt et al. 2014), SciPy (P. Virtanen et al. 2020), sigfig, Six, Sorted Containers, Soup Sieve, stack_data, Starburst99 (C. Leitherer et al. 1999), stsynphot (STScI Development

Team 2020; P. L. Lim et al. 2023), synphot, toolz, Tornado, Traitlets, tzdata, wcwidth, Zarr (A. Miles 2024).

Author Contributions

M.R.O. measured the Ly α parameters and $f_{\text{esc}}^{\text{LyC}}$ with advice from K.J.K., M.B.B., and T.E.R.-T. M.R.O. prepared the manuscript with comments and input from all coauthors. M.B. obtained the MagE spectra, which were reduced by J.R.R. M.D.G. reduced the HST data. K.S. developed the lens model, created the source-plane reconstruction with ray-traced non-LyC-leaking apertures, and calculated the magnification of the MagE apertures. A.N. removed foreground contaminants from the HST imaging to properly estimate $f_{\text{esc}}^{\text{LyC}}$ and added details of this process to the manuscript. This relied upon PSF models created by M.F. with software written by M.D.G. J.G.B. contributed to the background modeling of the HST imaging. M.R.O. created the HST-based Ly α maps based upon software originally written by J.R.R. and SEDs made by G.K. with photometry measured by M.F. G.K. contributed details of the SED modeling to the manuscript.

Access

The software used to create the results of this paper—and the results themselves—are available freely and publicly on GitHub, including detailed documentation (M. R. Owens & J. R. Rigby 2024).

ORCID iDs

M. Riley Owens  <https://orcid.org/0000-0002-2862-307X>
 Keunho J. Kim  <https://orcid.org/0000-0001-6505-0293>
 Matthew B. Bayliss  <https://orcid.org/0000-0003-1074-4807>
 T. Emil Rivera-Thorsen  <https://orcid.org/0000-0002-9204-3256>
 Keren Sharon  <https://orcid.org/0000-0002-7559-0864>
 Jane R. Rigby  <https://orcid.org/0000-0002-7627-6551>
 Alexander Navarre  <https://orcid.org/0000-0001-7548-0473>
 Michael Florian  <https://orcid.org/0000-0001-5097-6755>
 Michael D. Gladders  <https://orcid.org/0000-0003-1370-5010>
 Jessica G. Burns  <https://orcid.org/0000-0002-4519-7738>
 Gourav Khullar  <https://orcid.org/0000-0002-3475-7648>
 John Chisholm  <https://orcid.org/0000-0002-0302-2577>
 Guillaume Mahler  <https://orcid.org/0000-0003-3266-2001>
 Håkon Dahle  <https://orcid.org/0000-0003-2200-5606>
 Christopher M. Malhas  <https://orcid.org/0009-0000-6300-6184>
 Brian Welch  <https://orcid.org/0000-0003-1815-0114>
 Taylor A. Hutchison  <https://orcid.org/0000-0001-6251-4988>
 Raven Gassis  <https://orcid.org/0009-0004-7337-7674>
 Suhyeon Choe  <https://orcid.org/0000-0003-1343-197X>
 Prasanna Adhikari  <https://orcid.org/0009-0003-3123-4897>

References

- Astropy Collaboration, Price-Whelan, A. M., Lim, P. L., et al. 2022, *ApJ*, 935, 167
 Astropy Collaboration, Price-Whelan, A. M., Sipőcz, B. M., et al. 2018, *AJ*, 156, 123
 Astropy Collaboration, Robitaille, T. P., Tollerud, E. J., et al. 2013, *A&A*, 558, A33
 Atek, H., Labbé, I., Furtak, L. J., et al. 2024, *Natur*, 626, 975
 Behrens, C., Dijkstra, M., & Niemeyer, J. C. 2014, *A&A*, 563, A77
 Bergvall, N., Zackrisson, E., Andersson, B. G., et al. 2006, *A&A*, 448, 513
 Bian, F., Fan, X., McGreer, I., Cai, Z., & Jiang, L. 2017, *ApJL*, 837, L12
 Bolton, J. S., & Haehnelt, M. G. 2007, *MNRAS*, 382, 325

- Borthakur, S., Heckman, T. M., Leitherer, C., & Overzier, R. A. 2014, *Sci*, **346**, 216
- Bouwens, R. J., Illingworth, G. D., Oesch, P. A., et al. 2015, *ApJ*, **811**, 140
- Bowen, I. S. 1934, *PASP*, **46**, 146
- Bradley, L., Deil, C., Ginsburg, A., et al. 2024a, *astropy/regions*: v0.9, Zenodo, doi:10.5281/zenodo.10967055
- Bradley, L., Sipőcz, B., Robitaille, T., et al. 2022, *astropy/photutils*: v1.5.0, Zenodo, doi:10.5281/zenodo.6825092
- Bradley, L., Sipőcz, B., Robitaille, T., et al. 2024b, *astropy/photutils*: v1.13.0, Zenodo, doi:10.5281/zenodo.12585239
- Bridge, J. S., Hayes, M., Melinder, J., et al. 2018, *ApJ*, **852**, 9
- Bunker, A. J., Saxena, A., Cameron, A. J., et al. 2023, *A&A*, **677**, A88
- Byler, N., Dalcanton, J. J., Conroy, C., & Johnson, B. D. 2017, *ApJ*, **840**, 44
- Cao, X., Li, R., Shu, Y., et al. 2020, *MNRAS*, **499**, 3610
- Chamba, N., Knapen, J. H., & Black, D. 2022, *NatAs*, **6**, 1015
- Chisholm, J., Rigby, J. R., Bayliss, M., et al. 2019, *ApJ*, **882**, 182
- Choe, S., Rivera-Thorsen, T. E., Dahle, H., et al. 2024, arXiv:2405.06953
- Conroy, C., & Gunn, J. E. 2010, *ApJ*, **712**, 833
- Dahle, H., Aghanim, N., Guennou, L., et al. 2016, *A&A*, **590**, L4
- Dayal, P., Volonteri, M., Greene, J. E., et al. 2024, arXiv:2401.11242
- de Barros, S., Vanzella, E., Amorín, R., et al. 2016, *A&A*, **585**, A51
- Diego, J. M., Pascale, M., Kavanagh, B. J., et al. 2022, *A&A*, **665**, A134
- Dijkstra, M. 2017, arXiv:1704.03416
- Dijkstra, M., Gronke, M., & Venkatesan, A. 2016, *ApJ*, **828**, 71
- Draine, B. T. 2011, *Physics of the Interstellar and Intergalactic Medium* (Princeton, NJ: Princeton Univ. Press)
- Endsley, R., Stark, D. P., Whittler, L., et al. 2024, *MNRAS*, **533**, 1111
- Fletcher, T. J., Tang, M., Robertson, B. E., et al. 2019, *ApJ*, **878**, 87
- Flury, S. R., Jaskot, A. E., Ferguson, H. C., et al. 2022a, *ApJS*, **260**, 1
- Flury, S. R., Jaskot, A. E., Ferguson, H. C., et al. 2022b, *ApJ*, **930**, 126
- Foreman-Mackey, D., Hogg, D. W., Lang, D., & Goodman, J. 2013, *PASP*, **125**, 306
- Gazagnes, S., Chisholm, J., Schaerer, D., Verhamme, A., & Izotov, Y. 2020, *A&A*, **639**, A85
- Gnedin, N. Y., Kravtsov, A. V., & Chen, H.-W. 2008, *ApJ*, **672**, 765
- Grazian, A., Giallongo, E., Gerbasi, R., et al. 2016, *A&A*, **585**, A48
- Grazian, A., Giallongo, E., Paris, D., et al. 2017, *A&A*, **602**, A18
- Green, G. M., Schlafly, E. F., Finkbeiner, D. P., et al. 2015, *ApJ*, **810**, 25
- Guaia, L., Pentericci, L., Grazian, A., et al. 2016, *A&A*, **587**, A133
- Harris, C. R., Millman, K. J., van der Walt, S. J., et al. 2020, *Natur*, **585**, 357
- Hashimoto, T., Ouchi, M., Shimasaku, K., et al. 2017, *MNRAS*, **465**, 1543
- Hayes, M., Östlin, G., Duval, F., et al. 2014, *ApJ*, **782**, 6
- Herenz, E. C., Gruyters, P., Orlitova, I., et al. 2016, *A&A*, **587**, A78
- Hunter, J. D. 2007, *CSE*, **9**, 90
- Inoue, A. K., Shimizu, I., Iwata, I., & Tanaka, M. 2014, *MNRAS*, **442**, 1805
- Izotov, Y. I., Chisholm, J., Worseck, G., et al. 2022, *MNRAS*, **515**, 2864
- Izotov, Y. I., Guseva, N. G., Fricke, K. J., & Henkel, C. 2016a, *MNRAS*, **462**, 4427
- Izotov, Y. I., Guseva, N. G., Fricke, K. J., & Henkel, C. 2019a, *A&A*, **623**, A40
- Izotov, Y. I., Guseva, N. G., Fricke, K. J., Henkel, C., & Schaerer, D. 2017a, *MNRAS*, **467**, 4118
- Izotov, Y. I., Guseva, N. G., Fricke, K. J., et al. 2021a, *A&A*, **646**, A138
- Izotov, Y. I., Guseva, N. G., & Thuan, T. X. 2011, *ApJ*, **728**, 161
- Izotov, Y. I., Orlitová, I., Schaerer, D., et al. 2016b, *Natur*, **529**, 178
- Izotov, Y. I., Schaerer, D., Thuan, T. X., et al. 2016c, *MNRAS*, **461**, 3683
- Izotov, Y. I., Schaerer, D., Worseck, G., et al. 2018a, *MNRAS*, **474**, 4514
- Izotov, Y. I., Schaerer, D., Worseck, G., et al. 2020, *MNRAS*, **491**, 468
- Izotov, Y. I., Thuan, T. X., & Guseva, N. G. 2017b, *MNRAS*, **471**, 548
- Izotov, Y. I., Thuan, T. X., & Guseva, N. G. 2019b, *MNRAS*, **483**, 5491
- Izotov, Y. I., Thuan, T. X., Guseva, N. G., & Liss, S. E. 2018b, *MNRAS*, **473**, 1956
- Izotov, Y. I., Worseck, G., Schaerer, D., et al. 2021b, *MNRAS*, **503**, 1734
- Izotov, Y. I., Worseck, G., Schaerer, D., et al. 2021c, *MNRAS*, **503**, 1734
- Izotov, Y. I., Worseck, G., Schaerer, D., et al. 2018c, *MNRAS*, **478**, 4851
- Jaskot, A. E., Dowd, T., Oey, M. S., Scarlata, C., & McKinney, J. 2019, *ApJ*, **885**, A6
- Ji, Z., Giavalisco, M., Vanzella, E., et al. 2020, *ApJ*, **888**, 109
- Johnson, B., Foreman-Mackey, D., Sick, J., et al. 2022, *dfm/python-fsps*: python-fsps v0.4.2rc1, Zenodo, doi:10.5281/zenodo.7113363
- Johnson, B. D., Leja, J., Conroy, C., & Speagle, J. S. 2021, *ApJS*, **254**, 22
- Jones, L. H., Barger, A. J., & Cowie, L. L. 2021, *ApJ*, **908**, 222
- Kakiichi, K., & Gronke, M. 2021, *ApJ*, **908**, 30
- Kannan, R., Garaldi, E., Smith, A., et al. 2022, *MNRAS*, **511**, A005
- Kerutt, J., Wisotzki, L., Verhamme, A., et al. 2022, *A&A*, **659**, A183
- Khaira, V., Srianand, R., Choudhury, T. R., & Gaikwad, P. 2016, *MNRAS*, **457**, 4051
- Kim, J.-G., Kim, W.-T., & Ostriker, E. C. 2019, *ApJ*, **883**, 102
- Kim, K. J., Bayliss, M. B., Rigby, J. R., et al. 2023, *ApJL*, **955**, L17
- Kimm, T., Bieri, R., Geen, S., et al. 2022, *ApJS*, **259**, 21
- Kimm, T., Katz, H., Haehnelt, M., et al. 2017, *MNRAS*, **466**, 4826
- Kluyver, T., Ragan-Kelley, B., Pérez, F., et al. 2016, in *Positioning and Power in Academic Publishing: Players, Agents and Agendas*, ed. F. Loizides & B. Schmidt (Amsterdam: IOS Press), 87
- Knapen, J. H., Chamba, N., & Black, D. 2022, *NatAs*, **6**, 1021
- Kocevski, D. D., Onoue, M., Inayoshi, K., et al. 2023, *ApJL*, **954**, L4
- Kramarenko, I. G., Kerutt, J., Verhamme, A., et al. 2024, *MNRAS*, **527**, 9853
- Kroupa, P. 2001, *MNRAS*, **322**, 231
- Kuhlen, M., & Faucher-Giguere, C.-A. 2012, *MNRAS*, **423**, 862
- Lam, S. K., Pitrou, A., & Seibert, S. 2015, in *Proc. Second Workshop on the LLVM Compiler Infrastructure in HPC, LLVM '15* (New York: ACM)
- Leitet, E., Bergvall, N., Hayes, M., Linné, S., & Zackrisson, E. 2013, *A&A*, **553**, A106
- Leitet, E., Bergvall, N., Piskunov, N., & Andersson, B. G. 2011, *A&A*, **532**, A107
- Leitherer, C., Hernandez, S., Lee, J. C., & Oey, M. S. 2016, *ApJ*, **823**, 64
- Leitherer, C., Schaerer, D., Goldader, J. D., et al. 1999, *ApJS*, **123**, 3
- Lim, P. L., Rendina, M., Desjardins, T., et al. 2023, *spacetelescope/stsynphot_refactor*: 1.3.0 Release Notes, v1.3.0, Zenodo, doi:10.5281/zenodo.10215294
- Lin, Y.-H., Scarlata, C., Williams, H., et al. 2024, *MNRAS*, **527**, 4173
- Ma, X., Kasen, D., Hopkins, P. F., et al. 2015, *MNRAS*, **453**, 960
- Ma, X., Quataert, E., Wetzel, A., et al. 2020, *MNRAS*, **498**, 2001
- Madau, P., & Haardt, F. 2015, *ApJL*, **813**, L8
- Mainali, R., Rigby, J. R., Chisholm, J., et al. 2022, *ApJ*, **940**, 160
- Maji, M., Verhamme, A., Rosdahl, J., et al. 2022, *A&A*, **663**, A66
- Malkan, M. A., & Malkan, B. K. 2021, *ApJ*, **909**, 92
- Mallery, R. P., Mobasher, B., Capak, P., et al. 2012, *ApJ*, **760**, 128
- Marques-Chaves, R., Perez-Fournon, I., Shu, Y., et al. 2020, *MNRAS*, **492**, 1257
- Marques-Chaves, R., Schaerer, D., Alvarez-Marquez, J., et al. 2021, *MNRAS*, **507**, 524
- Marques-Chaves, R., Schaerer, D., Alvarez-Marquez, J., et al. 2022, *MNRAS*, **517**, 2972
- Marshall, J. L., Bures, S., Thompson, I. B., et al. 2008, *Proc. SPIE*, **7014**, 701454
- McKinney, W. 2010, in *9th Python in Science Conf.*, ed. S. van der Walt, **56**
- Mascia, S., Pentericci, L., & Calabrò, A. 2023, *A&A*, **672**, A155
- Masters, D., Capak, P., Salvato, M., et al. 2012, *ApJ*, **755**, 169
- Melinder, J., Östlin, G., Hayes, M., et al. 2023, *ApJS*, **266**, 15
- Mestric, U., Ryan-Weber, E. V., Cooke, J., et al. 2020, *MNRAS*, **494**, 4986
- Mestric, U., Vanzella, E., Upadhyaya, A., et al. 2023, *A&A*, **673**, A50
- Miles, A., Jakirkham, Bussonnier, M., et al. 2024, *zarr-developers/zarr-python*: v2.18.2, Zenodo, doi:10.5281/zenodo.11320255
- Mitra, S., Choudhury, T. R., & Ferrara, A. 2015, *MNRAS*, **454**, L76
- Mostardi, R. E., Shapley, A. E., Steidel, C. C., et al. 2015, *ApJ*, **810**, 107
- Murray, A., van Kemenade, H., wiredfool, A., et al. 2024, *python-pillow/Pillow*: v10.4.0, Zenodo, doi:10.5281/zenodo.12606429
- Naidu, R. P., Matthee, J., Oesch, P. A., et al. 2022, *MNRAS*, **510**, 4582
- Östlin, G., Hayes, M., Duval, F., et al. 2014, *ApJ*, **797**, 11
- Ouchi, M., Mobasher, B., Shimasaku, K., et al. 2009, *ApJ*, **706**, 1136
- Owens, M. R., & Rigby, J. R. 2024, Software release for 'Connecting Lyman- α and Ionizing Photon Escape in the Sunburst Arc', v2.0.1, Zenodo, doi:10.5281/zenodo.13888517
- Pahl, A. J., Shapley, A., Steidel, C. C., Reddy, N. A., & Chen, Y. 2022, *MNRAS*, **516**, 2062
- Pahl, A. J., Shapley, A., Steidel, C. C., et al. 2023, *MNRAS*, **521**, 3247
- Palanque-Desabrouille, N., Magneville, C., Yèche, C., et al. 2013, *A&A*, **551**, A29
- Pascale, M., & Dai, L. 2024, *ApJ*, **976**, 166
- Pascale, M., Dai, L., McKee, C. F., & Tsang, B. T. H. 2023, *ApJ*, **957**, 77
- Peng, C. Y., Ho, L. C., Impey, C. D., & Rix, H.-W. 2010, *AJ*, **139**, 2097
- Perez, F., & Granger, B. E. 2007, *CSE*, **9**, 21
- Pignataro, G. V., Bergamini, P., Meneghetti, M., et al. 2021, *A&A*, **655**, A81
- Planck Collaboration, Adam, R., Aghanim, N., et al. 2016, *A&A*, **596**, A108
- Price, L. C., Trac, H., & Cen, R. 2016, arXiv:1605.03970
- Puschnig, J., Hayes, M., Östlin, G., et al. 2017, *MNRAS*, **469**, 3252
- Rasekh, A., Melinder, J., Östlin, G., et al. 2022, *A&A*, **662**, A64
- Ricci, F., Marchesi, S., Shankar, F., La Franca, F., & Civano, F. 2017, *MNRAS*, **465**, 1915
- Rigby, J. R., Bayliss, M. B., Sharon, K., et al. 2018, *AJ*, **155**, 104

- Rivera-Thorsen, T. E., Dahle, H., Chisholm, J., et al. 2019, *Sci*, **366**, 738
- Rivera-Thorsen, T. E., Dahle, H., Gronke, M., et al. 2017, *A&A*, **608**, L4
- Rivera-Thorsen, T. E., Hayes, M., & Melinder, J. 2022, *A&A*, **666**, A145
- Rivera-Thorsen, T. E., Hayes, M., Östlin, G., et al. 2015, *ApJ*, **805**, 14
- Robertson, B. E. 2022, *ARA&A*, **60**, 121
- Robertson, B. E., Ellis, R. S., Furlanetto, S. R., & Dunlop, J. S. 2015, *ApJL*, **802**, L19
- Robertson, B. E., Furlanetto, S. R., Schneider, E., et al. 2013, *ApJ*, **768**, 71
- Robitaille, T., Lim, P. L., van Kerkwijk, M., & Starkman, N. 2024, *astropy/astropy-iers-data*: v0.2024.08.12.00.32.58, Zenodo, doi:10.5281/zenodo.13294985
- Rutkowski, M. J., Scarlata, C., Haardt, F., et al. 2016, *ApJ*, **819**, 81
- Rutkowski, M. J., Scarlata, C., Henry, A., et al. 2017, *ApJL*, **841**, L27
- Saha, K., Tandon, S. N., Simmonds, C., et al. 2020, *NatAs*, **4**, 1185
- Saldana-Lopez, A., Schaerer, D., Chisholm, J., et al. 2022, *A&A*, **663**, A59
- Sandberg, A., Östlin, G., Melinder, J., Bik, A., & Guaita, L. 2015, *ApJL*, **814**, L10
- Saxena, A., Pentericci, L., Ellis, R. S., et al. 2022, *MNRAS*, **511**, 120
- Schaerer, D., Marques-Chaves, R., Barrufet, L., et al. 2022, *A&A*, **665**, L4
- Shapley, A. E., Steidel, C. C., Strom, A. L., et al. 2016, *ApJL*, **826**, L24
- Sharma, M., Theuns, T., Frenk, C., et al. 2016, *MNRAS*, **458**, L94
- Sharon, K., Mahler, G., Rivera-Thorsen, T. E., et al. 2022, *ApJ*, **941**, 203
- Simcoe, R. A., Burgasser, A. J., Schechter, P. L., et al. 2013, *PASP*, **125**, 270
- Solhaug, E., Chen, H. W., Chen, M. C., et al. 2024, arXiv:2409.10604
- Steidel, C. C., Bogosavljević, M., Shapley, A. E., et al. 2018, *ApJ*, **869**, 123
- STScI Development Team 2020, *stsynphot*: synphot for HST and JWST, Astrophysics Source Code Library, ascl:2010.003
- The Matplotlib Development Team 2024, *Matplotlib*: Visualization with Python, v3.9.2, Zenodo, doi:10.5281/zenodo.13308876
- The pandas development team 2024, *pandas-dev/pandas*: Pandas, v2.2.2, doi:10.5281/zenodo.10957263
- U, V., Hemmati, S., Darvish, B., et al. 2015, *ApJ*, **815**, 57
- van der Walt, S. J., Schönberger, J. L., Nunez-Iglesias, J., et al. 2014, *PeerJ*, **2**, e453
- Vanzella, E., Caminha, G. B., Calura, F., et al. 2020a, *MNRAS*, **491**, 1093
- Vanzella, E., Castellano, M., Bergamini, P., et al. 2022, *A&A*, **659**, A2
- Vanzella, E., Giavalisco, M., Inoue, A. K., et al. 2010, *ApJ*, **725**, 1011
- Vanzella, E., Meneghetti, M., Pastorello, A., et al. 2020b, *MNRAS*, **499**, L67
- Vanzella, E., Nonino, M., Cupani, G., et al. 2018, *MNRAS*, **476**, L15
- Vasei, K., Siana, B., Shapley, A. E., et al. 2016, *ApJ*, **831**, 38
- Verhamme, A., Garel, T., Ventou, E., et al. 2018, *MNRAS*, **478**, L60
- Verhamme, A., Orlicová, I., Schaerer, D., & Hayes, M. 2015, *A&A*, **578**, A7
- Verhamme, A., Orlicová, I., Schaerer, D., et al. 2017, *A&A*, **597**, A13
- Verhamme, A., Schaerer, D., & Maselli, A. 2006, *A&A*, **460**, 397
- Virtanen, P., Gommers, R., Oliphant, T. E., et al. 2020, *NatMe*, **17**, 261
- Williams, H., Kelly, P. L., Chen, W., et al. 2023, *Sci*, **380**, 416
- Yang, H., Malhotra, S., Gronke, M., et al. 2017, *ApJ*, **844**, 171